Chemical Engineering Journal 507 (2025) 160641

Contents lists available at ScienceDirect

Chemical Engineering Journal

journal homepage: www.elsevier.com/locate/cej

Spinel-type high-entropy oxides for enhanced oxygen evolution reaction activity in anion exchange membrane water electrolyzers☆

Manuela Montalto [a], Williane da Silva Freitas [a,*], Emanuela Mastronardo [b], Valerio C.A. Ficca [c], Ernesto Placidi [c], Vincenzo Baglio [d], Erminia Mosca [d], Carmelo Lo Vecchio [d], Irene Gatto [d], Barbara Mecheri [a,*], Alessandra D'Epifanio [a]

[a] Department of Chemical Science and Technologies, University of Rome Tor Vergata, Via della Ricerca Scientifica 1, 00133 Rome, Italy
[b] Department of Engineering, University of Messina, C.da di Dio 98166, Messina, Italy
[c] Department of Physics, Sapienza University of Rome, Piazzale Aldo Moro 2, 00185 Rome, Italy
[d] Istituto di Tecnologie Avanzate per l'Energia, Nicola Giordano, CNR-ITAE, Salita Santa Lucia sopra Contesse, 5, 98126 Messina, Italy

ARTICLE INFO

Keywords:
High-entropy oxides
Spinel structure modulation
Oxygen evolution reaction
Rotating disk electrode study
Anion exchange membrane water electrolyzers

ABSTRACT

Developing efficient and cost-effective approaches to synthesize platinum group metal-free (PGM-free) electrocatalysts with high performance toward the sluggish oxygen evolution reaction (OER) is crucial for commercializing anion exchange membrane water electrolyzers (AEMWEs) to produce green hydrogen. Here, we propose a facile method to produce an emergent family of catalysts for the OER at the anode of AEMWEs. Spinel-type high entropy oxides (HEOs) based on Mg, Ni, Co, Mn, and Fe were synthesized by different methods, room-temperature or hydrothermal-assisted coprecipitation, using different coprecipitating agents (NH_3 solution *vs.* urea) and calcination conditions. Furthermore, HEO composition was tailored by modulating the metal's stoichiometry. Rietveld refinement and high-resolution transmission electron microscopy, coupled with energy-dispersive X-ray spectroscopy (HRTEM-EDX), indicated that single-phase HEOs with highly crystalline nanoparticles and homogeneous distribution of the metals were obtained by coprecipitation at room temperatures using NH_3, combined with the rapid quenching of the HEOs after treatment at 750 °C. Notably, the catalyst's performance was significantly enhanced (E_{J10} = 1.62 V *vs.* RHE), modulating the content of Ni, Co, and Mn, promoting their surface reconstruction and activation during OER with the formation of (oxy)hydroxides. AEMWE single-cell tests were carried out by integrating the optimized HEO as an anode catalyst of a catalyst-coated membrane, using the piperION® as a polymeric membrane and ionomer and Pt/C as a cathode catalyst. A remarkable performance was indicated with a high current density (J = 1.57 Acm^{-2}) at 1.8 V, with a maximum value (J = 4.14 Acm^{-2}) being reached at 2.2 V, outperforming highly active PGM-free catalysts reported in the literature.

1. Introduction

Expanding activities from the industrial and transport sectors are the main reasons for the increasing depletion of fossil fuels. Due to their use, several environmental issues have motivated researchers to pursue alternative energy sources [1,2]. Hydrogen is a sustainable energy carrier that can reduce the dependence of both sectors on fossil fuels, and electrochemical water-splitting [3] is a key process to producing green hydrogen and contributing to reaching the net zero emission (NZE) targets [4,5].

Among the technologies currently available as water electrolyzers, such as traditional alkaline water electrolyzers (AWEs) and proton exchange membrane water electrolyzers (PEMWEs), anion exchange membrane water electrolyzers (AEMWEs) are emergent devices that combine different advantages of AWEs and PEMWEs [1,6–8]: AEMWEs operate at low temperatures (50 – 90 °C) and at high current densities. Using a polymeric membrane also promotes the production of high-purity hydrogen that can be stored under higher pressures. Furthermore, less alkaline solutions can be used as feeding electrolytes [9], allowing for higher life cycling and the possibility of effectively

☆ This article is part of a special issue entitled: 'HYCELTEC2024' published in Chemical Engineering Journal.

* Corresponding authors.
E-mail addresses: williane.freitas@uniroma2.it (W.S. Freitas), barbara.mecheri@uniroma2.it (B. Mecheri).

https://doi.org/10.1016/j.cej.2025.160641

Available online 16 February 2025

replacing the platinum-group-metal (PGM)-based electrodes with cost-effective and Earth-abundant electrocatalysts [10–16].

The oxygen evolution reaction (OER) at the anode of AEMWEs is a critical reaction limiting the widespread implementation of these devices. The OER comprises multiple electron transfer steps (pH > 7: $4OH^- \rightarrow O_2 + 2H_2O + 4e^-$) with different reaction intermediates, dictating the overall efficiency of electrochemical water-splitting [1,6]. PGM electrocatalysts such as RuO_2 and IrO_2 are the benchmark catalysts to boost the sluggish OER kinetics. However, their scarcity, high cost, and low durability [17,18] call for developing alternative PGM-free materials that meet high activity and durability under the AEMWE operating conditions.

Several families of transition metal-based electrocatalysts, such as phosphides, chalcogenides, alloys, layer-double-hydroxides, functional perovskites, and spinel oxides, have been reported with promising OER performance at the anode of AEMWEs [19–24].

Recently, much attention has been given to multi-component materials, such as high-entropy oxides (HEOs), composed of five or more metals in an equimolar or near-equimolar ratio incorporated in a single lattice. HEOs typically exhibit modulable composition and properties, the latter promoted by the synergistic effect between the metals [25,26]. Spinel-type HEOs have been reported as attractive as OER catalysts due to their promising activity, superior performance durability [27–29], and structural functionalities. Their properties can be tuned with the modulation of the composition and nature of the metals in the "A" and "B" sites of the AB_2O_4 system, as well as defects engineering [30–32]. The metals in the "A" and "B" sites are identified as active sites with distinct catalytic activities towards the OER. On these metal-active sites, the OER is expected to follow a lattice oxygen-mediated mechanism (LOM) [33,34]. Given the OER activity of the A and B sites, the metal distribution strongly influences performance. For binary spinels taken as reference, the distribution of metals in the octahedral ($M^{3+}O_6$) B and tetrahedral ($M^{2+}O_4$) A sites can be represented by the $(A_{1-\lambda}B_\lambda)_{Td}[A_\lambda B_{2-\lambda}]_{Oct}O_4$ formula where the λ (λ = 0–1) parameter reflects the inversion degree of the spinel structure. When λ equals 0, the spinel is characterized by a normal structure, whereas when λ equals 1, it adopts an inverse structure. The combination and nature of the metal cations and the synthesis conditions influence the degree of inversion [35].

Regarding the differences in catalytic activity of metal-based sites, the redox-active octahedral B sites have higher activity than the tetrahedral A sites. Both experimental and theoretical studies suggest that the electronic structure of the redox-active octahedral ($M^{3+}O_6$) B sites plays a crucial role in determining the OER activity of transition metal spinels. For example, the occupancy of octahedral cations affects the binding strength of OER intermediates. Co-, Mn-, and Ni-based oxides exhibit the highest activity toward OER. Specifically, Co and Ni at the octahedral B sites significantly boost OER performance. Moreover, the octahedral ($M^{3+}O_6$) B sites exhibit a higher degree of metal–oxygen (M−O) covalence compared to the tetrahedral ($M^{2+}O_4$) A sites due to the greater electronic charge shared between oxygen and the metal cation. The stronger hybridization between O 2p and metal 3d orbitals enhances OER activity by promoting electron transfer between the redox-active metal center and oxygen. These properties make the metals in octahedral positions the primary catalytic sites for OER in the spinel structure, ultimately dictating the OER activity and mechanism [35–37].

Furthermore, oxygen vacancies play a crucial role in the relationship between the structure and properties of these materials, particularly in their performance toward OER. They are essential for promoting lattice oxygen redox chemistry by modulating the relative band positions of the transition metal *n*d and O 2p bands. This modulation facilitates M−O covalency and enhances the diffusion of molecular oxygen within the lattice, further impacting the overall catalytic efficiency. [38,39].

HEOs composed of a combination of Co, Ni, Mn, Fe, Cr, Zn, Al, and Mg cations have been recently investigated for OER [40–43], with each metal having a distinct impact on the properties of the oxide. The Jahn–Teller (J-T) distortion promoted by Mn^{3+}, Fe^{4+}, and Ni^{3+} was found to directly affect the orbital-related electron structures in spinel oxides [44]. Particularly, Mn-based spinel oxides are prone to octahedral distortion (elongation of the *c* lattice parameter and consequent increasing Mn–O bonding length along the *z*-axis) due to the Jahn-Teller active Mn^{3+} ($t_{2g}^3e_g^1$) occupying the octahedral sites. Despite this tendency, the effect of J-T distortion on the OER activity of spinels is still under debate. Hirai et al. [45] show that the OER activity and performance durability of Mn^{3+}-based oxides increased with the suppression of the Jahn–Teller distortion. When such distortion is suppressed, e.g. increasing the Co content in the spinel composition, the splitting of the $Mn^{3+}e_g$ orbitals becomes smaller, and the electron occupying the $Mn^{3+}e_g$ orbital shifts to a higher energy level, making stronger the overlap of the antibonding $Mn^{3+}e_g$ orbitals with the O 2p orbitals of the oxygen-based adsorbates. Differently, Wei and coworkers concluded that the J-T effect on octahedral sites does not significantly affect the OER activity by analyzing various Mn-containing spinel catalysts [36]. Other studies also report that *in situ* J-T distortion of Mn-based spinel used as electrode for battery applications is one of the primary causes the electrode degradation over cycling due to the continuous phase transition from cubic ($c/a = 1$) to tetragonal ($c/a = 1.16$), which causes anisotropic volume changes compromising the AB_2O_4 structure [46,47]. Furthermore, incorporating Mn in the AB_2O_4 structure improved lattice compressibility and reduced crystallite size, increasing the catalytically active surface area [48]. The presence of Fe at surface sites in different transition metal-based spinel oxides seems to induce an elongation of the M−O bonds, facilitating enhanced adsorption of intermediates such as O* and OH* due to electron depletion at active sites, stabilizing reaction intermediates through synergistic electronic interactions, especially with Ni and Co [49,50]. Besides the transition metals, the non-catalytic Mg^{2+} contributed to the structural stability of spinel oxides for different applications since it does not undergo electrochemical changes [51–53]. Moreover, due to its tendency to occupy the tetrahedral sites, the presence of Mg^{2+} cation can be used to modulate the composition of the octahedral sites [51].

Despite the advantages of HEOs, complex and costly synthesis techniques are often considered the most effective strategies for producing single-phase HEOs. Nebulized spray and flame spray pyrolysis [54,55], carbothermal shock [56,57], and electrospun synthesis [58–60] offer high reactivity of precursors and enable rapid formation and precise control over the purity of the oxides; however, they require specific, expensive instrumentation, which limits the scalability of the synthesis. Therefore, optimizing simple, cost-effective synthesis methods for producing HEOs is essential for advancing the research and practical applications of this emerging class of functional materials.

Solid state [61] and mechanochemical synthesis, sol–gel process [62], hydrothermal [63], and coprecipitation methods [64,65] are reported as common approaches to obtain single, bi-, and trimetallic transition metal spinel oxides. Among them, coprecipitation and hydrothermal methods offer several advantages. They allow for utilizing different synthesis precursors to tune the oxide's properties and offer control over the composition and homogeneity of the oxides requiring lower temperatures and cost-effective experimental setups. In the coprecipitation method, the metal cations undergo simultaneous precipitation as hydroxides or other insoluble salts, almost maintaining the desired stoichiometric ratio of metals predicted for the final spinel structure. The synthesis is usually carried out in an aqueous solution at room or mild temperature [66]. Differently, in the hydrothermal method, the oxide precursors are obtained in a sealed, high-pressure vessel. The reaction takes place at temperatures typically between 100 and 300 °C and high pressures, which facilitates the formation of highly crystalline phases as compared to the coprecipitation method [63,67], mainly carried out under ambient pressure and temperature conditions. For both methods, aqueous solutions are usually used to synthesize the oxides precursors, whose nature (e.g., hydroxides, (oxy)hydroxides, and carbonates) depends on the coprecipitation agents, metal salts, solvents, pH, temperature, time and pressure involved [68–70].

Besides the synthesis method, the calcination conditions, such as temperature, oxygen partial pressure, and cooling rate, also play a crucial role in the phase homogeneity of multimetallic spinel oxides [71–74]. Temperatures lower than 1000 °C [75], rapid cooling rate [76], and quenching [57] of the oxides were found to mitigate phase separation and the transition into rock salts while also controlling grain growth and stabilizing the crystalline phase. Moreover, the rapid quenching step is auspicious for synthesizing multimetallic spinels, as the fast cooling (often achieved by exposure to air) helps preserve the high-temperature phase before compositional gradients can develop [77,78].

In this study, spinel-type HEOs composed of Mg, Mn, Fe, Co, and Ni were synthesized, with their OER activity in an alkaline environment enhanced through optimization of synthesis methods and metal stoichiometry. Hydrothermal and coprecipitation techniques were explored using different reaction setups, coprecipitation agents, and calcination conditions. Single-phase HEOs with a highly crystalline structure, uniform metal distribution, and excellent OER activity at pH 14 were achieved by combining the coprecipitation method with rapid quenching after calcination at 750 °C. The tailored composition of the HEOs effectively facilitated the formation of spinel structures capable of delivering outstanding performance under simulated operating conditions. The optimized approach can be considered a promising alternative for developing functional materials with exceptional electrocatalytic activity, as demonstrated by tests in an AEMWE single cell equipped with the $Mg_{0.35}Ni_{0.78}Co_{0.78}Mn_{0.79}Fe_{0.38}O_4$ HEO at the anode, using a PiperION® membrane.

2. Materials and methods

2.1. Materials

Magnesium nitrate hexahydrate ($Mg(NO_3)_2{\cdot}6H_2O$) (99 %), iron (III) nitrate nonahydrate ($Fe(NO_3)_3{\cdot}9H_2O$) (≥ 99 %), manganese (II) acetate tetrahydrate ($Mn(CH_3COO)_2{\cdot}4H_2O$) (≥ 99 %), cobalt (II) nitrate hexahydrate ($Co(NO_3)_2{\cdot}6H_2O$) (99 %), cetyltrimethylammonium bromide (CTAB) (≥ 98 %), *N, N*-Dimethylformamide (99.8.%) and Nafion solution (5 wt% in lower aliphatic alcohols and water, 15–20 %) were purchased from Sigma-Aldrich. Nickel (II) nitrate hexahydrate ($Ni(NO_3)_2{\cdot}6H_2O$) (99,4%) and urea (99.5 %) were supplied by VWR chemicals. Millipore water (Merk, 18.2 MΩ) was used for materials preparation and experiments.

2.2. Synthesis optimization of high entropy oxides

Two synthesis methods, M1 and M2, were investigated to optimize the preparation of spinel-type HEOs in an equimolar ratio of Mg, Mn, Fe, Co, and Ni (0.6 mol each). For method M1, the coprecipitation of the metal hydroxide precursors was conducted at room temperature and promoted using ammonia solution (25 wt%) as a precipitating agent. An equimolar amount of the metal nitrates was dissolved in deionized water at room temperature, and ammonia solution (14 mL) was added dropwise to the solution at a controlled rate (~ 3 $mLmin^{-1}$) to obtain a precipitate in a gel form. The obtained gel was further stirred at 100 °C for 4 h for solvent removal and dried at 80 °C in an oven for 8 h. The collected powders were calcined with a heating rate of 5 °C min^{-1} under airflow Then, samples were rapidly quenched from the furnace after 30 min. Fig. S1 shows a schematic for M1.

The M2 synthesis consists in the coprecipitation of the metal hydroxide precursors by using urea as a precipitating agent and a surfactant to encapsulate the metal ions in a micellar system. The metal precursors were synthesized in a hydrothermal reactor, and the procedure is detailed and summarized in the 1.1 section of the Supplementary material and Fig. S2, respectively. For each method (M1 and M2), two calcination temperatures were investigated, 750 and 900 °C, and the samples were labeled as follows: M1A, M2A (750 °C) and M1B, M2B (900 °C). In addition to the synthesis parameters, the effect of the metals' stoichiometry on the OER activity of the spinel oxides was also investigated. Table 1 reports the molar nominal content of the metals per HEO mole.

2.3. Physicochemical characterization

To investigate the weight losses during the calcination step of both precursors, obtained from M1 and M2, thermogravimetric analysis (TGA) was performed by using a thermogravimetric analyzer TGA/DSC Star System (Mettler Toledo), with a heating ramp from 25 to 1000 °C and a heating rate of 5 °Cmin^{-1} under airflow.

The crystalline structure of the prepared materials (M1A, M1B, M2A, and M2B) was investigated by performing powder X-ray diffraction (XRPD) analysis. The diffraction patterns were recorded using a Philips PW1730 diffractometer with Cu Kα radiation (λ = 1.5406 Å) source in the 2θ range of 10° − 80° and a D8 Advance Bruker diffractometer Bragg-Brentano theta-2theta configuration, with Cu Kα radiation source, 40 V, 40 mA, 0.05° s^{-1} scan rate, with a LYNXEYE detector. Rietveld refinement against the diffraction data was performed using the GSAS package to determine the average crystallographic characteristics. The cubic *Fd-3 m* structure of $MgMn_{1.5}Co_{0.5}O_4$ (PDF 04–022-5879) was used as the initial structure for the refinements. Refinement parameters were limited to lattice parameters and sample displacement, while Uiso, fraction, and atomic coordinates were fixed. Peak profile parameters were taken from an independent measurement using a corundum reference.

The morphology of the HEOs powders was investigated using a Leo Supra 35 field-emission scanning electron microscope (FE-SEM) (Carl Zeiss, Oberkochen, Germany).

High-resolution transmission electron microscopy (HR-TEM) and energy-dispersive X-ray spectroscopy (EDX) mapping images were obtained using a cold field transmission electron microscope (JEM-F200, Jeol, Japan) at an operating voltage of 200 kV.

The surface area of the samples was investigated through the Brunauer–Emmett–Teller (BET) method by acquiring N_2-adsorption/desorption isotherms using a Micromeritics® TriStar II Plus surface area analyzer. Before measurements, samples were dried for 8 h at 250 °C under vacuum, followed by a second degassing step under N_2 flow for 2 h at 250 °C to remove adsorbed molecules.

The actual stoichiometry of HEOs was determined by inductively coupled plasma optical emission spectroscopy (ICP-OES-Varian 710-ES). For the measurement, samples were dispersed in HNO_3 (65 %), under reflux, at 100 °C for 24 h. Then, the solution was diluted using deionized water to obtain a 5 wt%. HNO_3.

Surface analysis composition was quantified using X-ray photoelectron spectroscopy (XPS) in ultra-high vacuum (UHV, < 10^{-10} mBar), using a SPECS PHOIBOS 150 XPS system equipped with monochromatic Al Kα (1486.6 eV) X-ray source and 2D CMOS accurate counting detector. The system was calibrated using Au 4f at 84 eV. The powder samples were placed into a custom Molybdenum sample holder, and the analysis was performed to collect a complete survey and six different core levels in the high-resolution mode for each sample, namely O 1 s,

Table 1
Nominal stoichiometry of the prepared HEOs.

Sample $Mg_tFe_wMn_xNi_yCo_zO_4$	t (Mg)	w (Fe)	x (Mn)	y (Ni)	z (Co)
M1A, M2A M1B, M2B	0.6	0.6	0.6	0.6	0.6
M1C	0.5	0.5	0.5	0.5	**1.0**
M1D	0.5	0.5	0.5	**1.0**	0.5
M1E	0.5	0.5	**1.0**	0.5	0.5
M1F	0.5	**1.0**	0.5	0.5	0.5
M1G	**1.0**	0.5	0.5	0.5	0.5
M1H	0.3	0.3	**0.8**	**0.8**	**0.8**

Mg 1 s, Mn 2p, Fe 2p, Co 2p, and Ni 2p. The passing energy was set to 20 eV for all elements. Kolibrik KolXPD software was used for the deconvolution of the peaks.

2.4. Electrochemical characterization

Electrochemical characterization was performed in a standard three-electrode cell, using 1 M potassium hydroxide (KOH) solution as electrolyte, a rotating disk electrode (0.196 cm^2, RDE-AFE4R2GCPT, Pine Research Instrumentation) as working electrode (WE), a graphite rod as counter electrode (CE) and a saturated silver-silver chloride electrode (Ag/AgCl, 3.3 M KCl 373/SSG/6) as reference electrode (RE). The measurements were recorded with a VMP3 Potentiostat (Bio-Logic Science Instruments), controlled by a computer through EC-Lab V10.18 software. The potential values for all electrochemical tests were measured *vs*. Ag/AgCl (3.3 M KCl) and converted to the reversible hydrogen electrode (RHE) scale using the following equation: $E_{RHE} = E_{Ag/AgCl} + 0.197 + 0.059pH$. In the electrochemical analysis, the reported potentials were iR-compensated by measuring the ohmic resistance of the system using electrochemical impedance spectroscopy (EIS). A single-point high-frequency impedance measurement was conducted, and the voltage drop was compensated by 85 % using the Bio-Logic EC-Lab software, following previously reported procedures [79,80].

The WE was modified by depositing a catalyst ink prepared as follows: 3.6 mg of powder catalyst were dispersed in 455 μL of a Nafion/DMF solution (0.1 wt%), and the suspension was ultrasonicated for 1 h in an ice bath. Then, 5 μL of the ink solution was dropped onto the previously cleaned and polished glassy carbon electrode and dried in a convection oven at 40 °C for 6 min to obtain 0.20 $mgcm^{-2}$ catalyst loading.

Before the electrochemical measurements, the electrolyte (1.0 M KOH) was purged with N_2 for at least 20 min. Cyclic voltammetry (CV) experiments using an RDE in static configuration were performed from 1.0 to 1.8 V *vs*. RHE at a 10 mVs^{-1} potential scan rate. Linear sweep voltammetry (LSV) was performed from 1.0 to 1.8 V *vs*. RHE at a rotation speed of 1600 rpm and a 10 mVs^{-1} scan rate. According to previous studies [81–83], OER onset potential (E_{onset}) was estimated by drawing two tangent lines in the non-Faradaic zone and the Faradaic zone, taking as E_{onset} the value where these two tangents intersect. EIS analysis was carried out under hydrodynamic conditions (1600 rpm) over a frequency range of 50 MHz − 100 kHz with an amplitude of 10 mV. ZSimpWin impedance fitting software (AMETEK Scientific Instrument) was used to model the EIS spectra. The confidence interval of the parameters extrapolated from the electrochemical analysis was calculated using the standard error derived from the average of four independent measurements for each sample.

2.5. Membrane electrode assembly preparation and AEMWE tests

The Membrane-Electrode Assembly (MEA), with a geometrical active area of 5 cm^2, was realized by a cold assembling procedure. The anode ink, based on M1H electrocatalyst and 20 wt% of PiperION® ionomer, was applied by spray coating technique directly onto the commercial PiperION® membrane (thickness 40 μm) surface to realize a one-side catalyst-coated membrane (CCM). The catalyst loading was maintained at 2.5 ± 0.1 $mgcm^{-2}$. Afterward, a Ni felt (Bekaert), acting as a backing layer and current collector, was coupled to the anodic compartment.

The cathode electrode was made by mixing a commercial 40 wt% Platinum on carbon (Alfa Aesar) and a 20 wt% of PiperION® ionomer. The ink was sprayed onto a Sigracet 25-BC (SGL group) gas diffusion layer (GDL) to obtain a catalyst-coated electrode (CCE), with a Pt loading of 0.50 ± 0.05 $mgcm^{-2}$, as reported elsewhere [84]. Before the MEA realization, the CCE and CCM were exchanged in a 1 M KOH aqueous solution for 1 h. A 5 cm^2 single cell was used for the electrochemical characterization. The tests were performed at atmospheric pressure, in a temperature range between 30 and 80 °C, by feeding the anode side with an alkaline aqueous solution (1.0 M KOH) with a flow rate of 5 $mLmin^{-1}$. A potentiostat–galvanostat device, PGSTAT302N, equipped with an FRA module (Autolab), was used to perform the measurements. *J*-V curves were carried out at a scan rate of 5 mVs^{-1}. AC-impedance analysis was used to determine the cell resistance. The electrochemical impedance spectroscopy (EIS) measurements were performed under potentiostatic control (at a cell voltage of 1.8 V) in a frequency range between 10 kHz and 100 mHz by frequency sweeping in the single sine mode. The amplitude of the sinusoidal excitation signal was 0.01 V r.m.s. A short stability test was carried out by chronopotentiometric analysis, maintaining the current at 1 Acm^{-2} for 100 h.

3. Results and discussion

3.1. Synthesis method optimization

The thermal decomposition of the spinel precursors synthesized by both the coprecipitation method with an ammonia solution (M1) and by hydrothermal-assisted coprecipitation using urea as a precipitating agent (M2) was investigated by TGA. Fig. S3 shows that the main weight losses for the precursors synthesized by M1 and M2 correspond to hydroxide oxidation. For M1, the weight loss occurs between 100 and 240 °C, while for M2, it is observed between 190 and 380 °C, which agrees with the literature [85,86]. The subsequent weight loss occurring at higher temperatures (390–590 °C), evidenced for the sample prepared using urea, is due to carbonate decomposition [87,88].

The morphology of the prepared HEOs was investigated by SEM analysis (Fig. S4a-d). Larger particles were formed for M1B and M2B samples calcinated at 900 °C, as higher calcination temperatures promote crystallite growth [89–91]. When comparing the effect of the synthesis method on the specific surface area (SSA) estimated from BET analysis for the samples obtained at 750 °C (M1A and M2A), SSA is lower for the sample obtained by the hydrothermal method (8.3 m^2g^{-1} for M1A *vs.* 2.9 m^2g^{-1} for M2A). This is consistent with the higher crystallinity typically observed in samples prepared by hydrothermal, which involves elevated temperature and pressure conditions. In contrast, the coprecipitation method, where oxide precursors are obtained under ambient temperature and pressure, leads to lower crystallinity. The SSA values agree with those found in the literature for typical spinel-type bimetallic oxides and other HEOs [92–95].

The XRPD (Fig. 1a) confirms the formation of the spinel-type HEOs from the different synthesis methods and calcination, as indicated by the characteristic diffraction peaks at 2θ values of 18.4°, 30.4°, 35.7°, 37.4°, 43.4°, 54.0°, 57.6°, 63.2°, 74.8°, that are attributed to the planes (111), (220), (311), (222), (400), (422), (511), (440) and (533) respectively, predicted to a *Fd-3m* space group [85,93,96]. Despite similar morphology, the combination of the coprecipitation method using NH_4OH as a coprecipitating agent and the lower calcination temperature (750 °C) were effective in obtaining single-phase spinel-type HEOs while avoiding the formation of MgO (PDF 90–900-6404) secondary phases.

The performance of M1A, M1B, M2A, and M2B towards the OER was evaluated by recording LSV under hydrodynamic conditions (Fig. 1b) in terms of the potential required to achieve 10 $mAcm^{-2}$ current density per geometric area (E_{J10}), a conventional parameter corresponding to the current density expected at the anode of a solar-powered water electrolyzer, under 1 sun illumination, needed to a 10 % efficiency [79].

Given the tendency of Ni- and Co-based spinel oxides to undergo surface reconstruction, particularly when combined with Fe [97], the LSV curves for the first cycle are reported to investigate the impact of the adopted stoichiometries on the HEOs' activity toward the OER. During the first cycle, the influence of surface reconstruction, metal leaching, and composition changes is considered minimal or negligible, allowing

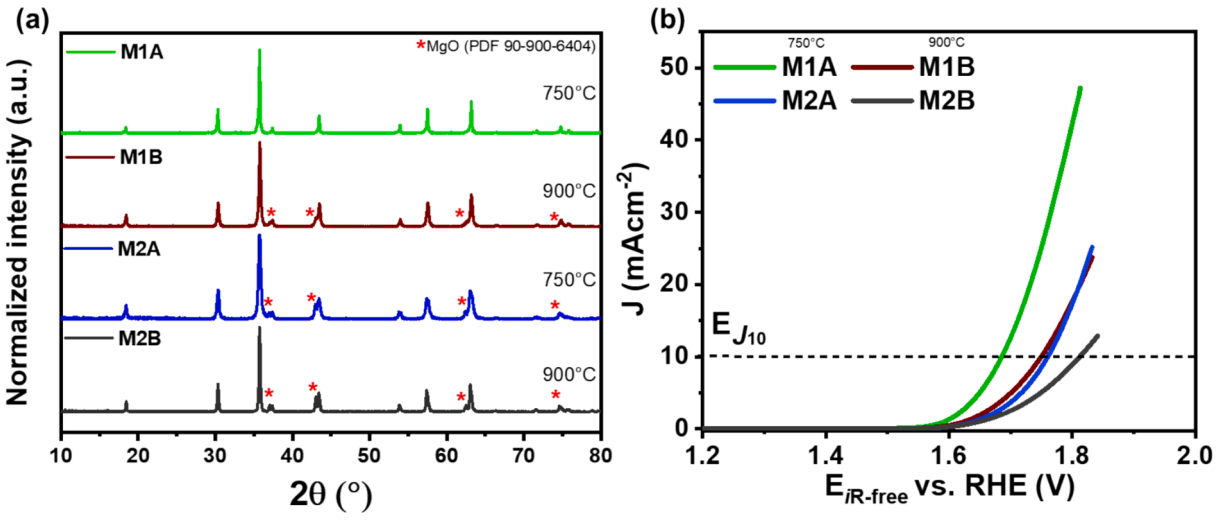

Fig. 1. (a) XRPD patterns, and (b) LSV curves recorded under N_2-saturated 1 M KOH at 1600 rpm and 10 mVs^{-1} with a 0.20 $mgcm^{-2}$ catalyst loading for the M1A, M2A, M1B, and M2B catalysts.

for a more straightforward assessment of composition-activity trends.

As indicated by Fig. 1b, the OER activity decreased with the increase in the calcination temperature, and it can be correlated to a larger particle size and a lower specific surface area of the samples obtained at 900 °C, together with the presence of MgO as a secondary phase. Higher OER activity is indicated for the M1A spinel oxide, with a lower onset potential (E_{onset} = 1.62 V *vs.* RHE) and E_{J10} (1.68 V *vs.* RHE). Furthermore, LSV curves were recorded to investigate the effect of the calcination time (0.5 h, 1 h, and 2 h) (Fig. S5) and the rapid quenching of the samples after calcination at 750 °C (Fig. S6) on the OER activity of the HEOs prepared by the coprecipitation method. Increasing the calcination time decreased the OER activity as indicated by higher E_{J10} values for the M1A-1 h and M1A-2 h; however, removing the samples from the heating zone to a room temperature zone of the furnace to a rapid quenching led to lower E_{J10}. As previously reported in the literature, quenching treatment on spinel oxides can increase their specific surface area, form abundant oxygen vacancies, and provide more active sites, improving their intrinsic catalytic activity [98,99].

3.2. Stoichiometry optimization of the high entropy oxides

Combining the coprecipitation method at room temperature with a lower calcination temperature (750 °C), followed by the rapid quenching of the samples, improved the OER activity of the HEOs; for these reasons, this method was adopted to prepare a series of five samples to investigate the effect of each metal by increasing their content from 0.6 to 1.0 mol at a time (Table 1).

XRPD patterns (Fig. 2a) for the M1C, M1D, M1E, M1F, and M1G samples show the typical diffraction peaks of the spinel structure. Moreover, M1C and M1D showed a pure single-phase, and magnesiowüstite (Mg, Fe)O (PDF 96–900-6045) is evidenced as a secondary phase for the samples M1E, M1F, and M1G, indicating that when the content of Mn, Fe, and Mg, respectively is increased incorporation of the five metal in a single lattice is compromised.

The formation of the (Mg, Fe)O secondary phase suggests either that a spinel-type HEO was obtained with a lower content of Mg and Fe or that the HEO was not effectively formed, resulting in spinel oxides with fewer than five metal cations in the structure. Both scenarios would alter the metal distribution between the octahedral ($M^{3+}O_6$) B and tetrahedral ($M^{2+}O_4$) A sites influencing the spinel's OER activity. Given that Mg^{2+} tends to occupy the tetrahedral sites and the higher catalytic activity of the octahedral sites as compared to the tetrahedral sites [35], the lower content of Mg^{2+} can limit the occupation of the octahedral ($M^{3+}O_6$) sites by the more active metals, such as Co, Ni, and Mn, thereby reducing the OER activity of the spinel-type HEOs. Additionally, single-metal or bimetallic oxides based on Mg and Fe exhibit poor OER activity,

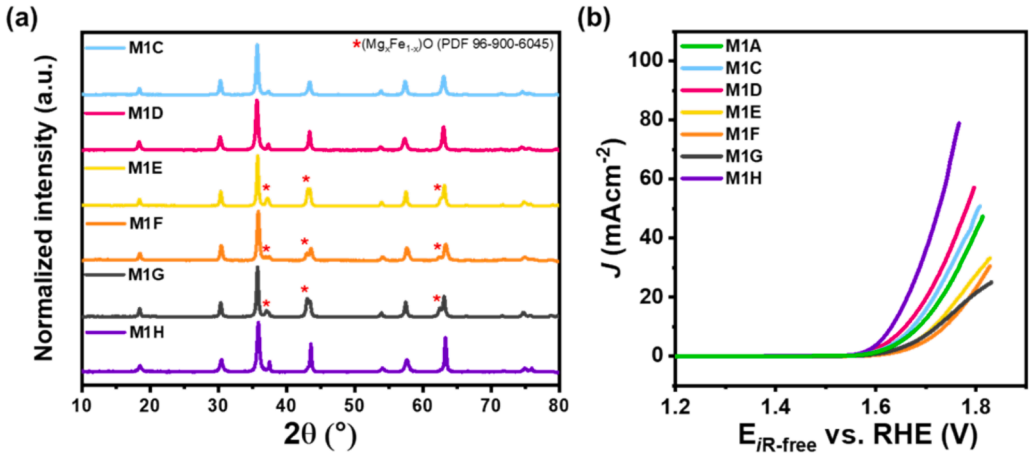

Fig. 2. (a) XRPD pattern and (b) LSV curves recorded under N_2-saturated 1 M KOH at 1600 rpm and 10 mVs^{-1}, with a 0.20 $mgcm^{-2}$ catalyst loading for the M1A, M1C, M1D, M1E, M1F, M1G and M1H catalysts.

and the presence of (Mg, Fe)O as a secondary phase may further compromise the catalyst's electrochemical stability [79,100].

The LSV curves for this series of HEOs (Fig. 2b) revealed that E_{J10} decreased for the M1C and M1D samples compared to M1A, while it increased for the M1E, M1F, and M1G samples. This trend can be attributed to the formation of secondary phases, specifically (Mg, Fe)O.

The increase of the nominal content of each metal to 1.0 mol at a time results in a performance increase according to the following trend: Ni > Co > Mn > Fe > Mg. The superior OER activity observed for M1C and M1D samples can be attributed to both the formation of a single-phase spinel-type HEO, allowing for the synergistic effect of the five metals on the catalytic activity, and the effect of a higher content of Co or Ni. Such metals are placed at the top of a Sabatier-type Volcano plot, delivering high OER activity as bimetallic oxides ($NiFeO_x$, $FeCoO_x$, $CoFeO_x$) [101].

To further modulate the electrochemical properties of the M1C and M1D catalyst while reducing the Co and Ni content, an HEO with a nominal content of 0.8 mol of Ni, Mn, and Co (M1H, $Mg_{0.3}Ni_{0.8-}Co_{0.8}Mn_{0.8}Fe_{0.3}O_4$) was prepared, and the achievement of a single-phase spine-type HEO indicated by the XRPD analysis (Fig. 2a). As shown in the polarization curves reported in Fig. 2b, the OER activity of the M1H significantly improved. For these reasons, the samples M1A, M1D, and M1H were taken as representative samples of the series for a deeper characterization.

The ICP-EOS analysis of M1A, M1D, and M1H indicates an actual stoichiometry comparable with the nominal content of each metal in the samples (Table 2).

Rietveld refinements results (Fig. 3) confirm the absence of secondary phase(s) and the formation of pure single-phase spinel. All the samples exhibit a cubic *Fd-3m* spinel structure. The unit cell and fitting parameters, data residual (R_{wp}), the R_{Bragg}, and Goodness of Fit (GOF) are also reported in Table 3. The increase of the Co and Mn content led to a decrease of the lattice parameters (M1D < M1A < M1H), with a 0.9 % cell volume contraction, which is supported by the slight intensity increase and narrowing of the diffraction peak at $2\theta = 63.3°$ (440 plane), indicating the formation of a more ordered spinel structure.

HR-TEM analysis (Fig. 4a-c) for the M1A, M1D, and M1H catalysts, respectively, showed the obtention of highly crystalline nanoparticles (20–150 nm) with well-defined interlayer distances (Fig. 4d-f and Fig. S7), in agreement with the XRPD data. Along with the formation of uniform and defined crystalline domains, the STEM-EDX elemental mapping (Fig. 4h-n and Figs. S8-S9) also indicated a homogeneous distribution of Mg, Mn, Fe, Ni, and Co over the spinel oxide structure in good agreement with the Rietveld refinements.

The surface chemistry of representative samples from the series (M1A, M1D, and M1H), before conditioning in the electrolyte and exposure to oxidative potentials during the OER, was investigated using XPS. This analysis aimed to identify the oxidation states of the metals at the surface of the HEOs and establish potential correlations between the proposed nominal stoichiometries and the metal oxidation states observed in the HEOs. Survey spectra are reported in Fig. 5a, while the high-resolution scans for identifying the Mg 1s, Ni 2p, Co 2p, Fe 2p, and Mn 2p core levels are shown in Fig. 5b-f and Figs. S10-S12. A summary of the XPS results is reported as follows, while a detailed description of the XPS analysis is provided in Section 2.6 of Supplementary material.

Surveys spectra (Fig. 5a) indicate, as expected, the presence of the six elements composing the spinel structure of M1A, M1D, and M1H samples, Ni, Co, Fe, Mn (600 – 900 eV), O (~530 eV, > 70 %) and Mg (1300 eV). The full elemental composition of samples can be found in Table S4.

The Mg 1s core levels (Fig. 5b and Fig. S10), with the highest binding energy (BE), are appreciated at a BE of 1304 eV, corresponding to a 2 + oxidation state [102,103]. For normal spinels, the occupation of the tetrahedral positions, the "A" sites of the AB_2O_4 system, has been attributed to divalent cations, while trivalent cations are prone to occupy octahedral positions, the "B" sites of the spinel structure. Differently, in inverse spinel, a fraction of the trivalent cations can replace the divalent in the tetrahedral positions [40,104]. In the case of spinel structures based on Mg, the Mg^{2+} are usually found to occupy the "A" sites (tetrahedral positions).

The Ni 2p core levels are reported in Fig. 5c and Fig. S11a-b. A maximum peak position at 855.6 eV is evidenced, with the characteristic satellite at *ca.* 861 eV corresponding to Ni^{2+} [105–107] being found as a single component (Rel.% = 100) for all the samples.

Deconvolution of the Co 2p core levels, Fig. 5d and Fig. S11c-d, show the main $2p_{3/2}$ line located at ~ 780.6 eV, corresponding to a Co^{2+} oxidation state, with the strong satellite at *ca.* 786 eV [108–110] found along with the weak satellite peak at 790 eV, which is indicative of the Co^{3+} whose the main $2p_{3/2}$ line is found at ~ 780 eV [109–111]. The presence of mixed oxidation states, Co^{2+} and Co^{3+}, with a higher contribution of Co^{2+} (> 60 %), is found for all samples. Furthermore, when the Co content related to the spinel structure increases, the contribution of Co^{2+} decreases. By comparing M1A with a lower Co content with M1H with a higher content of Co, Ni, and Mn, the relative percentage of Co^{3+} increased from 29 % to 37 % (Table S5), which can promote the incorporation of the Co^{3+} ions in the octahedral positions of the AB_2O_4 system.

The Fe 2p core levels are reported in Fig. 5e and Fig. S12a-b. The 2p spin–orbit splitting can be observed for all samples, with the satellite structures evident only for the $2p_{1/2}$ component at ~ 733 eV since the signal is buried under the noise created by the Auger transitions of Ni (L3M23M45 (^{1}P and ^{3}P)) between 700 and 720 eV and Co (L2M23M45 (^{1}P), L3M45M45) between 698 and 725 eV. The main peak is at ~ 712 eV, indicating a 3+ oxidation state. However, given the superposition of the abovementioned Auger lines, a mixed oxidation state (Fe^{2+} and Fe^{3+}), evidenced by the satellites around 715 eV for Fe(II) [112–114] and 720 eV for Fe(III) [112,115] was also considered. Chemical speciation of the Fe content (Table S5) showed that Fe^{3+} is the primary component in the samples M1A (Rel.% = 53) and M1H (Rel.% = 74), while it is Fe^{2+} (Rel.% = 56) for the M1D.

The 2p core levels of Mn are reported in Fig. 5f and Fig. S12c-d. Considering the BEs, two main peaks can be correlated to the two different oxidation states: Mn(II) at *ca.* 640.7 eV and Mn(III) at 642.2 eV. Indeed, regarding Mn(II), from the deconvolution, the assignment is due to the characteristic satellite found at *ca.* 645.2 eV. Regarding the peak at 642.2 eV, an upshifted 3+ oxidation state can be assumed due to charge-withdrawing effects promoted by the difference in electronegativity among the transition metals, with Mn possessing the lowest value and due to spectra' shape lacking the characteristic shoulder of Mn(IV) compounds [116,117]. A comparison of the Mn^{2+} and Mn^{3+} relative percentages for all samples shows a lower content of Mn^{3+} (Table S5) for the M1H sample. Once the "B" sites tend to be filled by trivalent ions in typical normal spinels, the lower content of Mn^{3+} in M1H can indicate a more pronounced incorporation of Mn in the "A" sites, promoting inversion of more OER active metals, such as Co^{3+} in the more catalytically active "B" sites.

Summarizing, samples M1A, M1D, and M1H are spinel oxides composed of transition metals with multiple oxidation states, prevalently in the 2+ and 3+ oxidation states. Mg and Ni were found in a 2+ oxidation state for all samples, and Co and Fe have been identified, assuming both 2+ and 3+ oxidation states. Co^{2+} and Mn^{3+} were the dominant forms in all HEOs investigated.

Since the oxygen vacancies were found to play an essential role in the

Table 2
Metal content (in moles) per mole of HEO, as determined by ICP-OES analysis for the M1A, M1D, and M1H samples.

Sample	Metal content (mol)				
	Mg	Fe	Mn	Ni	Co
M1A	0.71	0.67	0.72	0.61	0.69
M1D	0.62	0.56	0.54	0.94	0.52
M1H	0.35	0.38	0.79	0.78	0.78

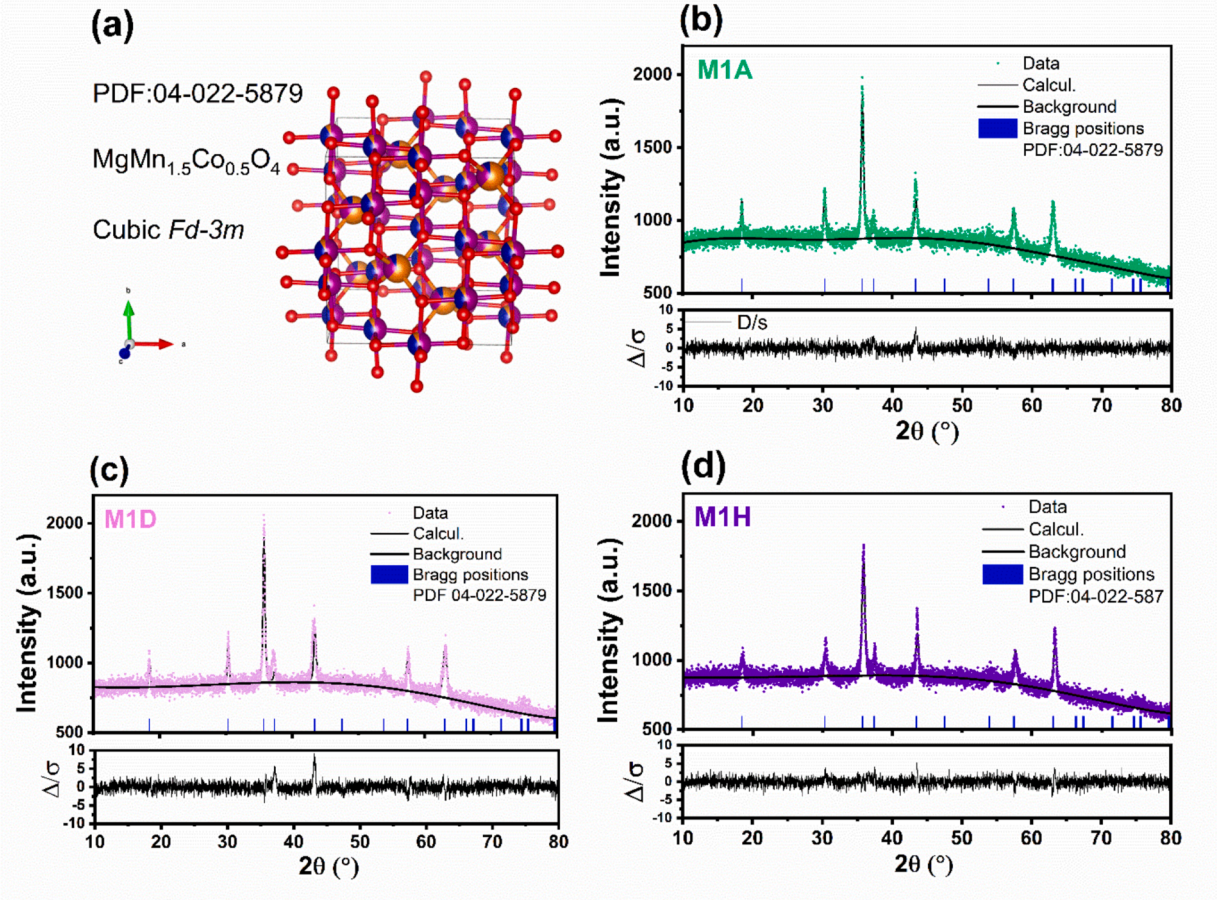

Fig. 3. (a) Reference cubic spinel structure for the Rietveld refinement; (b-d) Rietveld refinement results on the XRPD patterns for M1A, M1D, and M1H spinel-type high-entropy oxides.

Table 3
Unit cell parameters and indices from Rietveld refinements for M1A, M1D, and M1H samples.

Sample	Lattice parameters			Rietveld GOF
	a (Å)	V_{cell} (Å^3)	R_{wp}	
M1A	8.338(6)	579.68 ± 13	3.709	1.07
M1D	8.346(4)	581.35 ± 8	4.350	1.25
M1H	8.313(3)	574.48 ± 6	3.731	1.09

OER activity of different oxide families by promoting faster –OH adsorption from H_2O and the exposition of the metal active centers [118–121], the O 1s XPS spectra of the M1A, M1D, and M1H were deconvoluted to provide a semi-quantitative indication of their presence at the surface of the samples before the electrochemical activation. As illustrated in Fig. S13a-c, the O 1s spectra can be deconvoluted into three main components, typically ascribed to the O^{2-} ions arising from the oxide lattice (O_L) at *ca.* 530 eV; the surface hydroxyls groups (–OH) formed upon dissociatively adsorbed water and mostly considered as O^{2-} vacancies (O_V), at *ca.* 531 eV [122], and the adsorbed O_2 or H_2O identified with the components at higher binding energies (> 531.5 eV) [36,123]. Relative percentages between 20 and 30 % were obtained for the O_V component in the O 1 s XPS spectra of all samples (Table S5) following the trend: M1A (21.3 %) < M1D (26.5 %) < M1H (28.4 %), which indicates a higher contribute of the O_V component for the samples for the M1D and M1H HEOs, as compared to M1A with an equimolar content of the metals. It is worth highlighting that XPS analysis does not directly quantify the number of oxygen vacancies, requiring further analysis such as neutron powder diffraction [124], electron paramagnetic resonance (EPR) [119], *ex-situ* spectroscopic analysis such as X-ray absorption near edge structure (XANES) and X-ray absorption fine structure (EXAFS) [125] to confirm or refute the indication of the vacancies presence as well as the metals distribution in the "A" and "B" sites of the AB_2O_4 structure, both affecting the activity of the catalysts towards the OER.

LSV curves were recorded over 60 cycles for the M1D and M1H catalysts, which exhibited the highest OER activity within the HEOs series, to investigate performance variations during anodic polarization. As shown in Fig. 6, the performance of samples changes over the potential cycling; at the first LSV cycle, the catalysts show a more pronounced difference in terms of E_{onset} and the E_{J10}, with the M1H indicating higher performance than M1D. However, LSV curves become similar (E_{J10} = 1.64 ± 0.02–1.63 ± 0.01 V for M1D *vs.* 1.63 ± 0.01–1.62 ± 0.03 V for M1H) between the 30th and 60th cycles (Fig. 6a).

Performance enhancement of both HEOs can be primarily ascribed to the formation of Ni- and Co-based (oxy)hydroxides as indicated in the CV and LSV in hydrodynamic conditions recorded over cycling (Fig. 6b). The formation of (oxy)hydroxides is indicated by the appearance of the $Ni(OH)_2$/NiOOH (Ni^{2+}/Ni^{3+}) redox process in the potential region 1.3–1.45 V *vs.* RHE [126–130] and also by the contribution of $Co(OH)_2$/CoOOH and (Co^{3+}/Co^{4+}) redox peaks in the potential region 1.3 to 1.6 V [48,49,55]. The latter is not appreciable since it is located in the range with the oxidation process overlapping the Ni oxidation and the onset potential for the OER. According to reported studies in the literature, both performance improvement and its convergence over time for the M1D and M1H catalysts can account for different phenomena, including the evidenced formation of highly active (oxy)hydroxides [131–133] and metal leaching. The transition metals, particularly Fe in alkaline

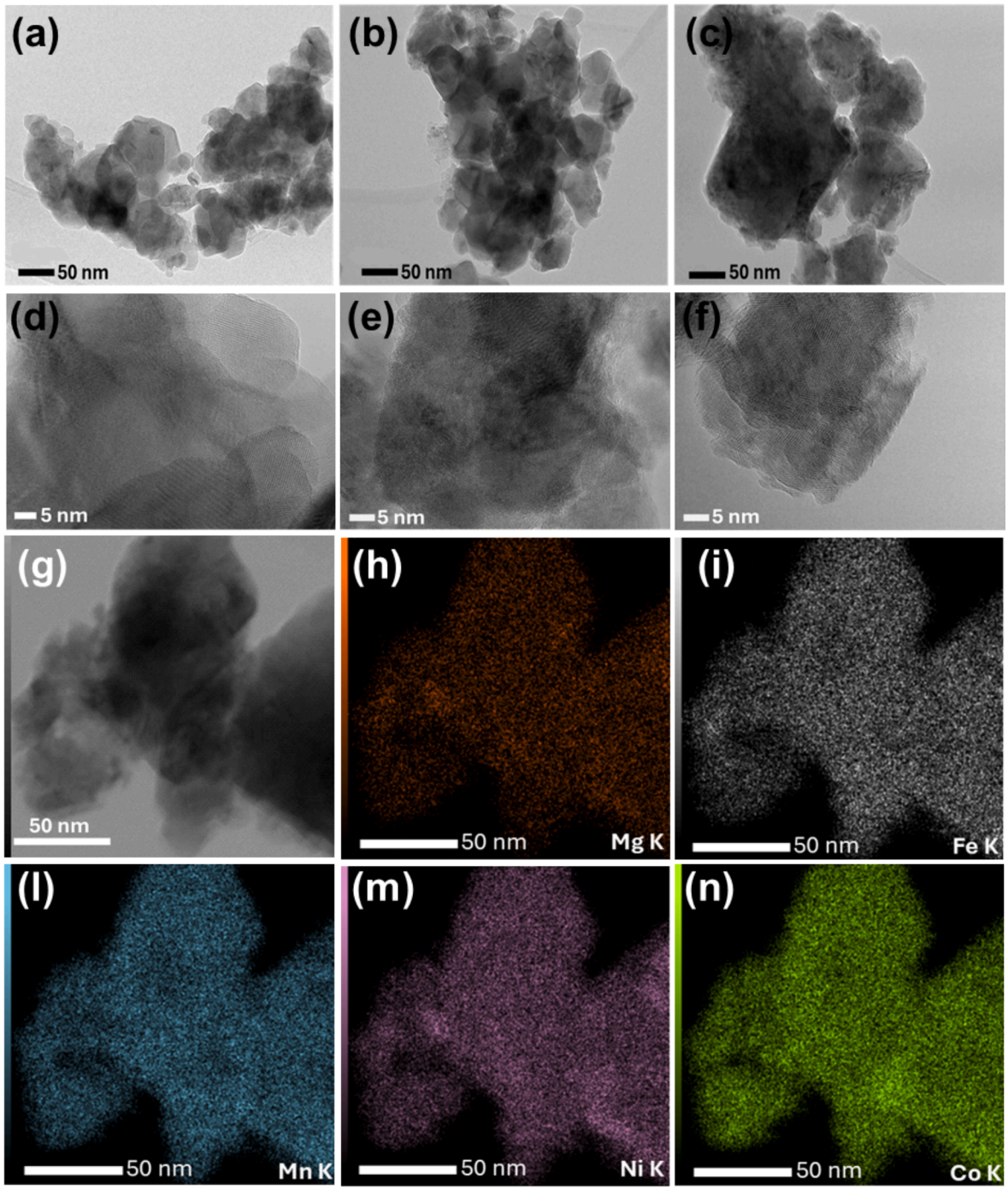

Fig. 4. HR-TEM images for (a) M1A, (b) M1D, (c) M1H at 120 kX, magnification at 800 kX for (d) M1A, (e) M1D, (f) M1H, with visible crystalline fringes, and (h-n) STEM-EDX of the M1H elemental mapping at 200 kX magnification region showed in (g).

electrolytes, are prone to dissolution [134–136], and the (oxy)hydroxide formation can facilitate this phenomenon affecting the catalyst's activity. Indeed, metal leaching can promote the exposition of the metal-based active sites of oxides [137], with the Fe leaching triggering surface reconstruction and being able to its reincorporation by *in situ* formed $Ni(OH)_2$/NiOOH and $Co(OH)_2$/CoOOH, increasing the OER activity [138–140].

Additionally, EIS and Tafel analysis were carried out for M1D, M1H, and M1A taken as a control to further investigate the catalysts activity and OER mechanism. Fig. 6c shows the Nyquist plots recorded at η_{J10} and hydrodynamic conditions. A single Randles-type equivalent circuit (EC) was used to model the impedance spectra of M1A, M1D, and M1H. The EC model includes the electrolyte resistance (R_s), the charge transfer resistance (R_{ct}), and a frequency-dependent constant phase element (Q). The calculated R_{ct} values decrease following the order: M1A > M1D > M1H (48 ± 4, 35 ± 4, and 15 ± 3 Ω, respectively), in agreement with the LSV analysis, highlighting that OER kinetics is promoted by faster charge transfer at the surface of the M1H catalyst.

Tafel analysis was performed to investigate the OER activity and mechanism. The Tafel plot is reported in Fig. 6d and linearly fitted after the E_{onset} between 1.56 and 1.61 V *vs.* RHE. Tafel slope values ranging between 40–65 $mVdec^{-1}$ were found for the M1A, M1D, and M1H catalysts, with the lower value observed for M1H, supporting the superior activity of the sample [141,142]. Lower Tafel slopes (30–60 $mVdec^{-1}$)

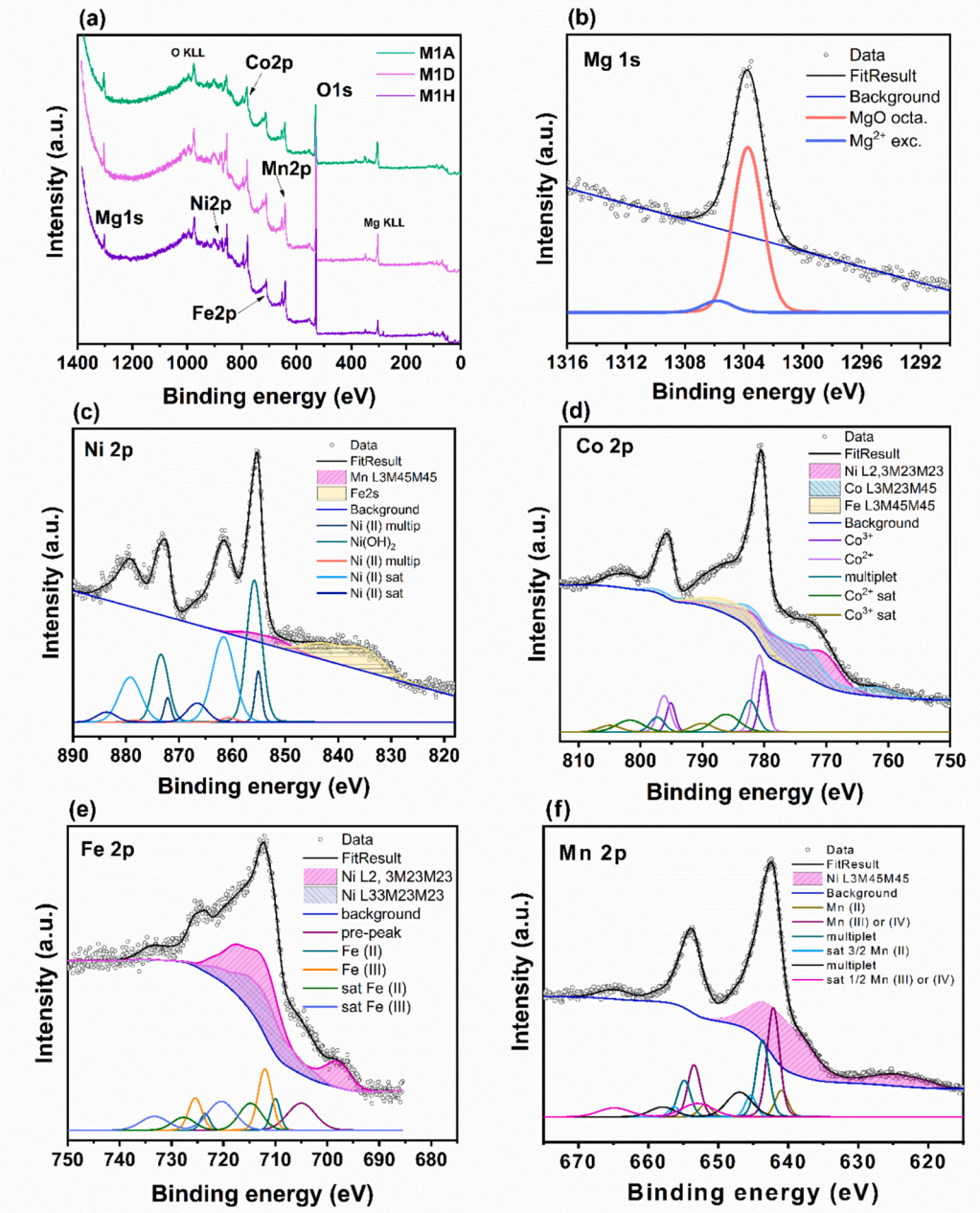

Fig. 5. (a) Survey XPS spectra for M1A, M1D and M1H, (b) Mg 1s, (c) Ni 2p, (d) Co 2p, (e) Fe 2p and (f) Mn 2p core levels for M1H.

are expected for OER proceeding on metal oxides following a lattice oxygen mechanism (LOM) [33] that contributes to the formation of oxygen vacancies in the lattice, which becomes a new active site. The LOM has been mainly identified in transition metal oxides such as perovskites and spinels [34,38,143].

The OER mechanism relies on the nature of the O atoms involved in the O-O bond formation. According to the spectroscopical and electrochemical studies reported for highly-active (oxy)hydroxides-based electrocatalysts, the observed Tafel slopes can be related to LOM with an *rds* (rate determining step) described by the release of O_2 from M−superoxide intermediate ($MOO^- \rightleftharpoons M + O_2 + e^-$) [144,145], (see equation 5 in Table S2) indicating that the deprotonation of surface hydroxide and O-O bond formation steps [38,144] are kinetically promoted on the HEOs' surface. It can be ascribed to the *in-situ* formed Ni- and Co-based (oxy)hydroxides upon the surface reconstruction evidenced from the electrochemical tests (Fig. 6b), highlighting the high OER activity of M1D and M1H, which was competitive in comparison to other HEOs and conventional oxides reported in the literature (Table S3) [27,43,55,146].

3.3. AEMWE tests

Given the superior OER activity demonstrated in the half-cell tests, the M1H ($Mg_{0.35}Ni_{0.78}Co_{0.78}Mn_{0.79}Fe_{0.38}O_4$) catalyst was tested at the anode side of a 5 cm^2 electrolysis cell. The MEA was prepared by spraying the M1H catalyst (mixed with the ionomer) onto the PiperION® membrane, which was integrated with a gas diffusion electrode loaded with a Pt/C catalyst composing the cathode. A 1 M KOH solution was supplied to the anode compartment of the cell at a flow rate of 5 $mLmin^{-1}$.

Fig. 7a reports the *J*-V curves recorded at different temperatures between 30 and 80 °C. As the temperature increases, the water-splitting onset potential decreases, and the current density increases due to the increased ionic conductivity of the AEM (decrease in series resistance,

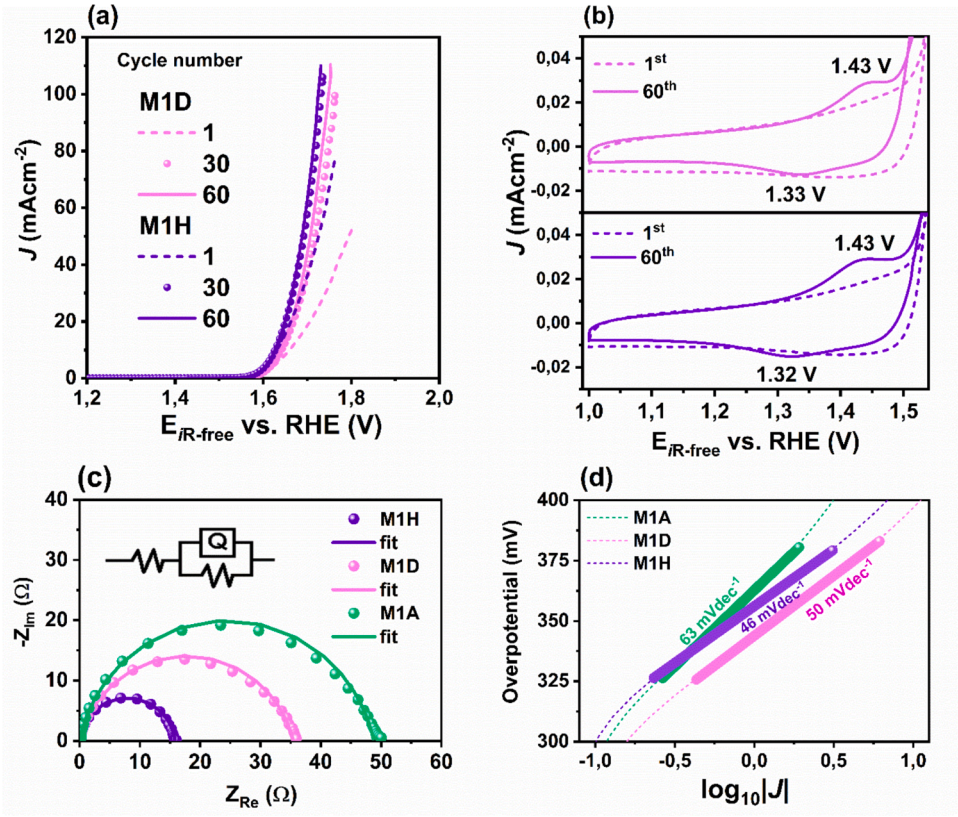

Fig. 6. (a) LSV-RDE curves and (b) 1st and 60th CV cycle for M1D (pink) and M1H (purple), (c) Nyquist plots obtained at η_{J10} with the equivalent circuit as an inset, and (d) Tafel plot for M1A, M1D, and M1H samples. (For interpretation of the references to colour in this figure legend, the reader is referred to the web version of this article.)

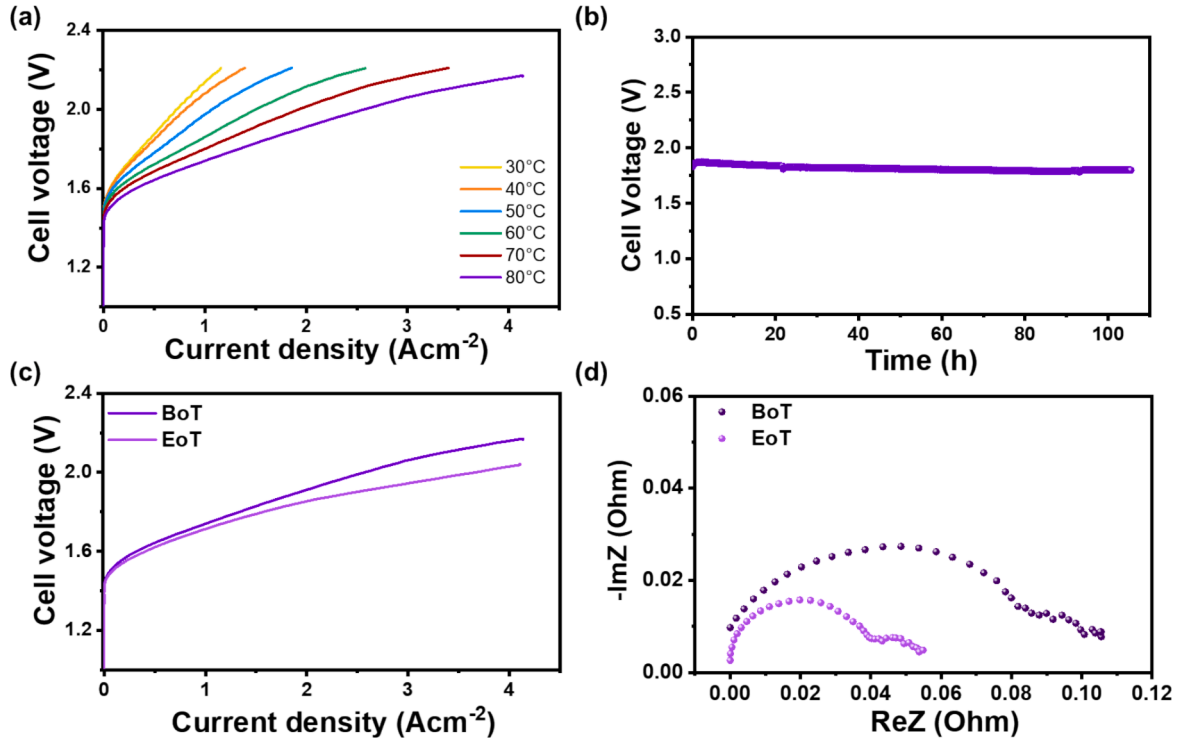

Fig. 7. (a) Polarization curves recorded at different temperatures, (b) chronopotentiometry test recorded at 1 Acm^{-2} and 80 °C, (c) polarization curves, and (d) EIS recorded beginning (BoT) and end (EoT) of durability test for a 5 cm^2 AEMWE single-cell equipped with the M1H catalyst at the anode and using PiperION® (40 μm tick) membrane.

R_s, in the Nyquist plot) and faster kinetic at the electrodes (decrease in charge transfer resistance, R_{ct}), as shown in Fig. S14 [147]. A maximum current density of 4.1 Acm^{-2} was reached at 2.2 V, while at a lower voltage of 1.8 V, a 1.57 Acm^{-2} current density was delivered. The obtained performance appears superior to that observed for AEMWEs equipped with similar PGM-free at the anode, as reported in Table 4, although different membranes and catalyst characteristics are present. For this reason, a comparison with the current literature is not straightforward. However, achieving high performance is not the primary objective when a catalyst is designed and prepared; durability is also critical for AEMWE development.

A short-term (*ca.* 100 h) durability test under galvanostatic operating conditions (1 A cm^{-2}) was performed, and the obtained chronopotentiometry curve is reported in Fig. 7b. After a slight increase in initial potential, the curve shows a voltage decrease over time until around 95 h of operation. This stable behavior over time is evidence of the catalyst's OER activity, which demonstrates not only high performance but also exceptional stability. *J*-V and EIS plots (Fig. 7c-d) after this short-term durability test (end of test, EoT) show even higher performance (1.57 Acm^{-2} at 1.8 V) compared with the beginning of the test (BoT), mainly due to a decreased charge transfer kinetics (R_{ct}) (Fig. 7d), that can be ascribed as a possible contribution of the surface reconstruction and metal leaching over time. The performance durability of the AEMWE equipped with the M1H catalysts at the anode is also comparable to or even higher than other oxides-based anodes reported in the literature (Table S6).

4. Conclusions

The synthesis of spinel-type HEOs composed of Mg, Ni, Co, Fe, and Mn was optimized by investigating different methods for obtaining the HEOs precursors. Two precipitating agents and calcination conditions were investigated. A facile approach combining ammonia to form the hydroxide precursors at room temperature, together with a calcination step at 750 °C, and the rapid quenching of the sample after the heat treatment allows for obtaining catalysts with high OER activity in an alkaline medium (1 M KOH, pH = 14).

Furthermore, different stoichiometries were investigated, and the modulation of Mg, Fe, Ni, Co, and Mn content significantly enhanced the catalyst's performance. Rietveld refinement and STEM-EDX analysis confirmed the obtention of a spinel single-phase with highly crystalline nanoparticles (20–150 nm) and a homogeneous distribution of all metals. The chemical surface analysis (XPS) of the HEOs showed that Mg and Ni are found as 2 + ions, with Co, Fe, and Mn assuming 2+/3 + oxidation states. LSV-RDE tests showed that Ni and Co were more effective in enhancing the OER performance (E_{J10} = 1.64 and 1.62 V for M1D and M1H, respectively), and an increase in their content promoted the formation of highly active Ni- and Co-based (oxy)hydroxides upon surface reconstruction during anodic polarization. The activity of the spinel oxides as pre-catalysts is directly influenced by the octahedral positions of the AB_2O_4 structure, oxygen vacancies, and the formation of (oxy)hydroxides, along with possible metal leaching. To gain deeper insights into the metal distribution, potential oxygen vacancies, composition changes during oxidative potential cycling, and the OER mechanism, further characterization combining *ex-situ* and *in-operando* XAS (e.g., XANES and EXAFS) measurements can be explored. The synthesized M1H ($Mg_{0.35}Ni_{0.78}Co_{0.78}Mn_{0.79}Fe_{0.38}O_4$) showed promising catalytic activity towards OER, quite comparable to other HEOs obtained by multistep synthesis approaches and conventional oxides reported in the literature. When integrated at the anode of an AEMWE using a CCM approach to investigate its application, high performance was evidenced in terms of a current density at 1.8 V (~ 1.57 A cm^{-2}) and durability over time (~ 100 h), outperforming AEMWEs cells reported in the literature with active Ru-free and Ru-based catalysts assembled at the anode. The obtained performance of the HEO-based CCM at 80 °C can be attributed to the high activity and durability of the high-entropy spinel oxide (M1H), as confirmed by the BoT and EoT *J*-V curves in good agreement with the half-cell tests. The combination of a facile synthesis method with a tailored optimization of the HEOs metal composition is highlighted in this study as a promising approach to the synthesis and optimization of an emergent class of functional transition-metal-based oxides as an alternative to RuO_2 at the anode of AEMWEs.

CRediT authorship contribution statement

Manuela Montalto: Writing – original draft, Investigation, Formal analysis, Data curation. **Williane da Silva Freitas:** Writing – review & editing, Writing – original draft, Supervision, Methodology, Investigation, Conceptualization. **Emanuela Mastronardo:** Writing – review & editing, Resources, Investigation, Formal analysis, Data curation. **Valerio C.A. Ficca:** Writing – original draft, Data curation. **Ernesto Placidi:** Writing – review & editing, Resources, Investigation, Formal analysis, Conceptualization. **Vincenzo Baglio:** Writing – review & editing, Resources, Methodology, Investigation. **Erminia Mosca:** Writing – original draft, Investigation, Data curation. **Carmelo Lo Vecchio:** Writing – original draft, Investigation, Data curation. **Irene Gatto:** Writing – review & editing, Resources, Methodology, Investigation. **Barbara Mecheri:** Writing – review & editing, Supervision, Resources, Project administration, Methodology, Conceptualization. **Alessandra D'Epifanio:** Writing – review & editing, Supervision, Resources, Project administration, Methodology, Funding acquisition, Conceptualization.

Declaration of competing interest

The authors declare that they have no known competing financial

Table 4
Performance comparison in terms of the current density values at two typical applied voltages adopted for AEMWE operation, using similar PGM-free catalysts at the anode.

Membrane	Anode	Cathode	Electrolyte	*J*@1.8 V (Acm^{-2})	*J*@2.0 V (Acm^{-2})	T (°C)	Ref.
PiperION® (40 μm)	HEO-M1H	Pt/C	1 M KOH	1.57	3.72	80	This work
PiperION® (40 μm)	HEO-M1H	Pt/C	1 M KOH	0.78	1.52	60	This work
FAA-3–50	$NiFe_2O_4$	Pt/C	1 M KOH	1.50	2.50	60	[8]
Sustainion X37-50 RT	HEO-NS	PtRu/C	1 M KOH	1.50	2.50	60	[148]
Sustainion X37-50 RT	CrFeCoNi oxide	PtRu/C	1 M KOH	1.20	2.10	60	[148]
FAA-3–50	$NiFe_2O_4$	Pt/C	1 M KOH	1.20	2.00	60	[147]
Sustainion X37-50 RT	FeCoNi oxide	PtRu/C	1 M KOH	1.00	1.80	60	[148]
Sustainion X37-50 Grade T	$(FeCoNiCrMnCu)_3O_4$	Pt/C	1 M KOH	1.00	2.10	50	[149]
FAA-3–50	$Ni_{0.5}Mn_{0.5}Co_2O_4$	Pt/C	1 M KOH	0.85	1.60	60	[150]
FAA-3–50	FeCoNi oxide	Pt/C	1 M KOH	0.85	1.85	60	[151]
FAA-3–50	g-CN-CNF-800	Pt/C	1 M KOH	0.48	0.98	60	[152]
PiperION-A60-HCO3	$CoCrO_x$	Pt/C	1 M KOH	0.44	0.90	60	[153]
PiperION (40 μm)	Ni-Foam	Pt/C	1 M KOH	0.38	0.87	60	[154]

interests or personal relationships that could have appeared to influence the work reported in this paper.

Acknowledgments

This work was partly supported by the Italian Ministry of Foreign Affairs and International Cooperation, grant number CN23GR06.

This work also received funding from the European Union – Next-GenerationEU – under the public notice of the Italian Ministry of University and Research (MUR) no. 3138 of 16/12/2021 and subsequent correction no. 3175 of 18/12/2021, Project No. CN00000023 MOST – Sustainable Mobility Center.

The XPS experiments were carried out at the SmartLab departmental laboratory of the Department of Physics at Sapienza University of Rome. EP and VCAF are grateful to Dr. Marco Sbroscia for technical assistance during the XPS measurements.

Appendix A. Supplementary data

Supplementary data to this article can be found online at https://doi.org/10.1016/j.cej.2025.160641.

Data availability

Data will be made available on request.

References

[1] M. Chatenet, B.G. Pollet, D.R. Dekel, F. Dionigi, J. Deseure, P. Millet, R.D. Braatz, M.Z. Bazant, M. Eikerling, I. Staffell, P. Balcombe, Y. Shao-Horn, H. Schäfer, Water electrolysis: from textbook knowledge to the latest scientific strategies and industrial developments, Chem. Soc. Rev. 51 (2022) 4583–4762, https://doi.org/10.1039/D0CS01079K.

[2] N.T. Suen, S.F. Hung, Q. Quan, N. Zhang, Y.J. Xu, H.M. Chen, Electrocatalysis for the oxygen evolution reaction: recent development and future perspectives, Chem. Soc. Rev. 46 (2017) 337–365, https://doi.org/10.1039/C6CS00328A.

[3] S. Dresp, F. Dionigi, M. Klingenhof, P. Strasser, Direct electrolytic splitting of seawater: Opportunities and challenges, ACS Energy Lett. 4 (2019) 933–942, https://doi.org/10.1021/acsenergylett.9B00220.

[4] M. van der Spek, C. Banet, C. Bauer, P. Gabrielli, W. Goldthorpe, M. Mazzotti, S. T. Munkejord, N.A. Røkke, N. Shah, N. Sunny, D. Sutter, J.M. Trusler, M. Gazzani, Perspective on the hydrogen economy as a pathway to reach net-zero CO 2 emissions in Europe, Energy, Environ. Sci. 15 (2022) 1034–1077, https://doi.org/10.1039/D1EE02118D.

[5] S.J. Davis, N.S. Lewis, M. Shaner, S. Aggarwal, D. Arent, I.L. Azevedo, S.M. Benson, T. Bradley, J. Brouwer, Y.M. Chiang, C.T.M. Clack, A. Cohen, S. Doig, J. Edmonds, P. Fennell, C.B. Field, B. Hannegan, B.M. Hodge, M.I. Hoffert, E. Ingersoll, P. Jaramillo, K.S. Lackner, K.J. Mach, M. Mastrandrea, J. Ogden, P.F. Peterson, D.L. Sanchez, D. Sperling, J. Stagner, J.E. Trancik, C.J. Yang, K. Caldeira, Net-zero emissions energy systems, Science (1979) 360 (2018). https://doi.org/10.1126/science.aas9793.

[6] C. Santoro, A. Lavacchi, P. Mustarelli, V. Di Noto, L. Elbaz, D.R. Dekel, F. Jaouen, What is Next in Anion-Exchange Membrane Water Electrolyzers? Bottlenecks, Benefits, and Future, ChemSusChem 15 (2022) e202200027 https://doi.org/10.1002/cssc.202200027.

[7] N. Carboni, L. Mazzapioda, A. Caprì, I. Gatto, A. Carbone, V. Baglio, M. A. Navarra, Composite anion exchange membranes based on graphene oxide for water electrolyzer applications, Electrochim. Acta 486 (2024) 144090, https://doi.org/10.1016/j.electacta.2024.144090.

[8] A. Caprì, I. Gatto, C. Lo Vecchio, S. Trocino, A. Carbone, V. Baglio, Anion Exchange Membrane Water Electrolysis Based on Nickel Ferrite Catalysts, ChemElectroChem 10 (2023) e202201056, https://doi.org/10.1002/celc.202201056.

[9] M. Yu, E. Budiyanto, H. Tüysüz, Principles of Water Electrolysis and Recent Progress in Cobalt-, Nickel-, and Iron-Based Oxides for the Oxygen Evolution Reaction, Angew. Chem. Int. Ed. 61 (2022) e202103824, https://doi.org/10.1002/anie.202103824.

[10] B. Ricciardi, B. Mecheri, W. da Silva Freitas, V.C.A. Ficca, E. Placidi, I. Gatto, A. Carbone, A. Capasso, A. D'Epifanio, Porous Iron-Nitrogen-Carbon Electrocatalysts for Anion Exchange Membrane Fuel Cells (AEMFC), ChemElectroChem 202201115 (2023) 1–12. https://doi.org/10.1002/celc.202201115.

[11] B. Ricciardi, W. da Silva Freitas, B. Mecheri, K.U. Nisa, J. Montero, V.C.A. Ficca, E. Placidi, C. Alegre, A. D'Epifanio, Hierarchical porous Fe/Ni-based bifunctional oxygen electrocatalysts for rechargeable zinc-air batteries, Carbon N Y 219 (2024) 118781. https://doi.org/10.1016/j.carbon.2023.118781.

[12] W. da Silva Freitas, A. D'Epifanio, C. Lo Vecchio, I. Gatto, V. Baglio, V.C.A. Ficca, E. Placidi, B. Mecheri, Tailoring MOF structure via iron decoration to enhance ORR in alkaline polymer electrolyte membrane fuel cells, Chemical Engineering Journal 465 (2023) 142987, https://doi.org/10.1016/j.cej.2023.142987.

[13] B. Ricciardi, S. Freitas, B. Mecheri, J. Manuel, C. Alegre, D. Sebastián, M. J. Lázaro, A.D. Epifanio, P-functionalization of Ni Fe - Electrocatalysts from Prussian Blue Analogue for Enhanced Anode in Anion Exchange Membrane Water Electrolysers, Chem. Eng. J. (2024) 156256, https://doi.org/10.1016/j.cej.2024.156256.

[14] W. da Silva Freitas, B. Mecheri, C. Lo Vecchio, I. Gatto, V. Baglio, V.C.A. Ficca, A. Patra, E. Placidi, A., D'Epifanio, Metal-organic-framework-derived electrocatalysts for alkaline polymer electrolyte fuel cells, J Power Sources 550 (2022) 232135, https://doi.org/10.1016/j.jpowsour.2022.232135.

[15] K.U. Nisa, W. da Silva Freitas, J. Montero, A. D'Epifanio, B. Mecheri, Development and Optimization of Air-Electrodes for Rechargeable Zn–Air Batteries, Catalysts 13 (2023), https://doi.org/10.3390/catal13101319.

[16] N. Wang, S. Song, W. Wu, Z. Deng, C. Tang, Bridging Laboratory Electrocatalysts with Industrially Relevant Alkaline Water Electrolyzers, Adv. Energy Mater. 14 (2024) 2303451, https://doi.org/10.1002/aenm.202303451.

[17] Y. Lin, Z. Tian, L. Zhang, J. Ma, Z. Jiang, B.J. Deibert, R. Ge, L. Chen, Chromium-ruthenium oxide solid solution electrocatalyst for highly efficient oxygen evolution reaction in acidic media, Nat. Commun. 10 (2019), https://doi.org/10.1038/S41467-018-08144-3.

[18] K. Du, L. Zhang, J. Shan, J. Guo, J. Mao, C.C. Yang, C.H. Wang, Z. Hu, T. Ling, Interface engineering breaks both stability and activity limits of RuO2 for sustainable water oxidation, Nat. Commun. 13 (2022), https://doi.org/10.1038/S41467-022-33150-x.

[19] D.H. Park, M.H. Kim, M. Kim, J.H. Byeon, J.S. Jang, J.H. Kim, D.M. Lim, S. H. Park, Y.H. Gu, J. Kim, K.W. Park, Spherical nickel doped cobalt phosphide as an anode catalyst for oxygen evolution reaction in alkaline media: From catalysis to system, Appl Catal B 327 (2023) 122444, https://doi.org/10.1016/j.apcatb.2023.122444.

[20] M. Mohamed Abouelela, G. Kawamura, A. Matsuda, Metal chalcogenide-based photoelectrodes for photoelectrochemical water splitting, Journal of Energy Chemistry 73 (2022) 189–213, https://doi.org/10.1016/j.jechem.2022.05.022.

[21] E. López-Fernández, C. Gómez-Sacedón, J. Gil-Rostra, J.P. Espinós, A. R. González-Elipe, F. Yubero, A. de Lucas-Consuegra, Ionomer-Free Nickel-Iron bimetallic electrodes for efficient anion exchange membrane water electrolysis, Chem. Eng. J. 433 (2022) 133774, https://doi.org/10.1016/j.cej.2021.133774.

[22] Y. Yang, W.H. Lie, R.R. Unocic, J.A. Yuwono, M. Klingenhof, T. Merzdorf, P. W. Buchheister, M. Kroschel, A. Walker, L.C. Gallington, L. Thomsen, P.V. Kumar, P. Strasser, J.A. Scott, N.M. Bedford, Defect-Promoted Ni-Based Layer Double Hydroxides with Enhanced Deprotonation Capability for Efficient Biomass Electrooxidation, Adv. Mater. 35 (2023) 2305573, https://doi.org/10.1002/adma.202305573.

[23] D. Chen, Y.S. Park, F. Liu, L. Fang, C. Duan, Hybrid perovskites as oxygen evolution electrocatalysts for high-performance anion exchange membrane water electrolyzers, Chem. Eng. J. 452 (2023) 139105, https://doi.org/10.1016/j.cej.2022.139105.

[24] H.J. Liu, S. Zhang, R.Y. Fan, B. Liu, R.Q. Lv, Y.M. Chai, B. Dong, Activated M,S co-doping (M = Ni, Co, Mn) inverse spinel oxides with mixed mechanisms for water oxidation, Appl Catal B 343 (2024) 123567, https://doi.org/10.1016/j.apcatb.2023.123567.

[25] H. Qiao, X. Wang, Q. Dong, H. Zheng, G. Chen, M. Hong, C.P. Yang, M. Wu, K. He, L. Hu, A high-entropy phosphate catalyst for oxygen evolution reaction, Nano Energy 86 (2021) 106029, https://doi.org/10.1016/j.nanoen.2021.106029.

[26] K.L. Svane, J. Rossmeisl, Theoretical Optimization of Compositions of High-Entropy Oxides for the Oxygen Evolution Reaction**, Angew. Chem. Int. Ed. 61 (2022) e202201146, https://doi.org/10.1002/anie.202201146.

[27] D. Wang, C. Duan, H. He, Z. Wang, R. Zheng, H. Sun, Y. Liu, C. Liu, Microwave solvothermal synthesis of Component-Tunable High-Entropy oxides as High-Efficient and stable electrocatalysts for oxygen evolution reaction, J. Colloid Interface Sci. 646 (2023) 89–97, https://doi.org/10.1016/j.jcis.2023.05.043.

[28] Q. Wang, J. Li, Y. Li, G. Shao, Z. Jia, B. Shen, Non-noble metal-based amorphous high-entropy oxides as efficient and reliable electrocatalysts for oxygen evolution reaction, Nano Res. 15 (2022) 8751–8759, https://doi.org/10.1007/S12274-022-4179-8.

[29] S. Jiang, K. Tian, X. Li, C.Q. Duan, D. Wang, Z. Wang, H. Sun, R. Zheng, Y. Liu, Amorphous High-entropy Non-precious metal oxides with surface reconstruction toward highly efficient and durable catalyst for oxygen evolution reaction, J. Colloid Interface Sci. 606 (2022) 635–644, https://doi.org/10.1016/j.jcis.2021.08.060.

[30] Ö.N. Avcl, L. Sementa, A. Fortunelli, Mechanisms of the Oxygen Evolution Reaction on NiFe2O4and CoFe2O4Inverse-Spinel Oxides, ACS Catal. 12 (2022) 9058–9073, https://doi.org/10.1021/acscatal.2C01534.

[31] L. Zhang, Q. Fan, K. Li, S. Zhang, X. Ma, First-row transition metal oxide oxygen evolution electrocatalysts: regulation strategies and mechanistic understandings, Sustain, Energy Fuels 4 (2020) 5417–5432, https://doi.org/10.1039/D0SE01087A.

[32] G. Janani, Y. Chae, S. Surendran, Y. Sim, W. Park, J.K. Kim, U. Sim, Rational Design of Spinel Oxide Nanocomposites with Tailored Electrochemical Oxygen Evolution and Reduction Reactions for ZincAir Batteries, Applied Sciences 2020, Vol. 10, Page 3165 10 (2020) 3165. https://doi.org/10.3390/app10093165.

[33] X. Xie, L. Du, L. Yan, S. Park, Y. Qiu, J. Sokolowski, W. Wang, Y. Shao, Oxygen Evolution Reaction in Alkaline Environment: Material Challenges and Solutions, Adv. Funct. Mater. 32 (2022) 2110036, https://doi.org/10.1002/adfm.202110036.

[34] Y. Sun, H. Liao, J. Wang, B. Chen, S. Sun, S.J.H. Ong, S. Xi, C. Diao, Y. Du, J.O. Wang, M.B.H. Breese, S. Li, H. Zhang, Z.J. Xu, Covalency competition dominates the water oxidation structure–activity relationship on spinel oxides, Nature Catalysis 2020 3:7 3 (2020) 554–563. https://doi.org/10.1038/s41929-020-0465-6.

[35] Y. Zhou, S. Sun, C. Wei, Y. Sun, P. Xi, Z. Feng, Z.J. Xu, Significance of Engineering the Octahedral Units to Promote the Oxygen Evolution Reaction of Spinel Oxides, Adv. Mater. 31 (2019) 1902509, https://doi.org/10.1002/adma.201902509.

[36] C. Wei, Z. Feng, G.G. Scherer, J. Barber, Y. Shao-Horn, Z.J. Xu, C. Wei, Z.J. Xu, Z. Feng, G.G. Scherer, J. Barber, Y. Shao-Horn, Cations in Octahedral Sites: A Descriptor for Oxygen Electrocatalysis on Transition-Metal Spinels, Adv. Mater. 29 (2017) 1606800, https://doi.org/10.1002/adma.201606800.

[37] M.S.A. Sher Shah, V.K. Paidi, H. Jung, S. Kim, G. Lee, J.W. Han, K.S. Lee, J. H. Park, Unprecedented electrocatalytic oxygen evolution performances by cobalt-incorporated molybdenum carbide microflowers with controlled charge re-distribution, J Mater Chem A Mater 9 (2021) 1770–1783, https://doi.org/10.1039/D0TA10915K.

[38] J.T. Mefford, X. Rong, A.M. Abakumov, W.G. Hardin, S. Dai, A.M. Kolpak, K.P. Johnston, K.J. Stevenson, Water electrolysis on La1−xSrxCoO3−δ perovskite electrocatalysts, Nature Communications 2016 7:1 7 (2016) 1–11. https://doi.org/10.1038/ncomms11053.

[39] H. Liu, X. Li, C. Peng, L. Zhu, Y. Zhang, H. Cheng, J. Cui, Q. Wu, Y. Zhang, Z. Chen, W. Zou, W. Gu, H. Huang, J. Wang, B. Ye, Z. Fu, Y. Lu, Activating the lattice oxygen in (Bi0.5Co0.5)2O3 by vacancy modulation for efficient electrochemical water oxidation, J Mater Chem A Mater 8 (2020) 13150–13159, https://doi.org/10.1039/D0TA03411H.

[40] C. Triolo, K. Moulaee, A. Ponti, G. Pagot, V. Di Noto, N. Pinna, G. Neri, S. Santangelo, Spinel-Structured High-Entropy Oxide Nanofibers as Electrocatalysts for Oxygen Evolution in Alkaline Solution: Effect of Metal Combination and Calcination Temperature, Adv. Funct. Mater. 34 (2024) 2306375, https://doi.org/10.1002/ADFM.202306375.

[41] P. Dadvari, W.H. Hung, K.W. Wang, High Entropy Spinel Oxide (AlCrCoNiFe2)O as Highly Active Oxygen Evolution Reaction Catalysts, ACS Omega 9 (2024) 27692–27698, https://doi.org/10.1021/acsomega.4C03807.

[42] R. Zhang, Z. Xu, Z. Du, Y. Wan, S. Yuan, F. Zeng, J. Xu, Z. Meng, X. Hu, H. Tian, Electrodeposition of Self-Supported High-Entropy Spinel Oxides for Stable Oxygen Evolution, Inorg. Chem. 62 (2023) 19052–19059, https://doi.org/10.1021/acs.inorgchem.3C02930.

[43] K. Iwase, I. Honma, High-Entropy Spinel Oxide Nanoparticles Synthesized via Supercritical Hydrothermal Processing as Oxygen Evolution Electrocatalysts, ACS Appl. Energy Mater. 5 (2022) 9292–9296, https://doi.org/10.1021/acsaem.2C01751.

[44] L. Zhao, C. Xin, C. Yu, Y. Xing, Z. Wei, H. Zhang, T. Fei, S. Liu, H. Zhang, T. Zhang, The Jahn–Teller distortion-induced electronic structure regulation of Mn-doped Co3O4 for enhanced acetone detection, InfoMat (2024) e12634, https://doi.org/10.1002/inf2.12634.

[45] S. Hirai, S. Yagi, A. Seno, M. Fujioka, T. Ohno, T. Matsuda, Enhancement of the oxygen evolution reaction in Mn3+-based electrocatalysts: correlation between Jahn–Teller distortion and catalytic activity, RSC Adv. 6 (2015) 2019–2023, https://doi.org/10.1039/C5RA22873E.

[46] X. Li, Y. Xu, C. Wang, Suppression of Jahn–Teller distortion of spinel LiMn2O4 cathode, J. Alloy. Compd. 479 (2009) 310–313, https://doi.org/10.1016/j.jallcom.2008.12.081.

[47] Y. Liu, C. Wang, S. Zhao, L. Zhang, K. Zhang, F. Li, J. Chen, Mitigation of Jahn–Teller distortion and Na+/vacancy ordering in a distorted manganese oxide cathode material by Li substitution, Chem. Sci. 12 (2021) 1062–1067, https://doi.org/10.1039/D0SC05427E.

[48] A.N. Naveen, S. Selladurai, Investigation on physiochemical properties of Mn substituted spinel cobalt oxide for supercapacitor applications, Electrochim. Acta 125 (2014) 404–414, https://doi.org/10.1016/j.electacta.2014.01.161.

[49] J. Baek, M.D. Hossain, P. Mukherjee, J. Lee, K.T. Winther, J. Leem, Y. Jiang, W.C. Chueh, M. Bajdich, X. Zheng, Synergistic effects of mixing and strain in high entropy spinel oxides for oxygen evolution reaction, Nature Communications 2023 14:1 14 (2023) 1–11. https://doi.org/10.1038/s41467-023-41359-7.

[50] T. Priamushko, P. Guggenberger, A. Mautner, J. Lee, R. Ryoo, F. Kleitz, Enhancing OER Activity of Ni/Co Oxides via Fe/Mn Substitution within Tailored Mesoporous Frameworks, ACS Appl. Energy Mater. 5 (2022) 13385–13397, https://doi.org/10.1021/acsaem.2C02055.

[51] S. Yang, L. Sun, Q. Li, T. Xia, L. Huo, H. Zhao, Optimizing the eg occupancy of magnesium cobalt spinel oxides via Fe substitution to promote oxygen evolution reaction, J. Alloy. Compd. 921 (2022) 166074, https://doi.org/10.1016/j.jallcom.2022.166074.

[52] C. Triolo, M. Maisuradze, M. Li, Y. Liu, A. Ponti, G. Pagot, V. Di Noto, G. Aquilanti, N. Pinna, M. Giorgetti, S. Santangelo, Charge Storage Mechanism in Electrospun Spinel-Structured High-Entropy (Mn0.2Fe0.2Co0.2Ni0.2Zn0.2)3O4 Oxide Nanofibers as Anode Material for Li-Ion Batteries, Small 19 (2023) 2304585, https://doi.org/10.1002/smll.202304585.

[53] K.H. Nam, Z. Wang, J. Luo, C. Huang, M.F. Millares, A. Pace, L. Wang, S.T. King, L. Ma, S. Ehrlich, J. Bai, E.S. Takeuchi, A.C. Marschilok, S. Yan, K.J. Takeuchi, M. M. Doeff, High-Entropy Spinel Oxide Ferrites for Battery Applications, Chem. Mater. 36 (2024) 4481–4494, https://doi.org/10.1021/acs.chemmater.4C00085.

[54] T.G. Brandt, A.R. Tuokkola, M. Yu, R.M. Laine, Liquid-feed flame spray pyrolysis enabled synthesis of Co- and Cr-free, high-entropy spinel oxides as Li-ion anodes, Chem. Eng. J. 474 (2023) 145495, https://doi.org/10.1016/j.cej.2023.145495.

[55] D. Stenzel, B. Zhou, C. Okafor, M.V. Kante, L. Lin, G. Melinte, T. Bergfeldt, M. Botros, H. Hahn, B. Breitung, S. Schweidler, High-entropy spinel-structure oxides as oxygen evolution reaction electrocatalyst, Front. Energy Res. 10 (2022) 942314, https://doi.org/10.3389/fenrg.2022.942314/.

[56] W. Liao, F. Qing, Q. Liu, R. Wu, C. Zhou, L. Chen, Y. Chen, X. Li, Carbothermal Shock Synthesis of Lattice Oxygen-Mediated High-Entropy FeCoNiCuMo-O Electrocatalyst with a Fast Kinetic, High Efficiency, and Stable Oxygen Evolution Reaction, Nano Lett. (2025), https://doi.org/10.1021/acs.nanolett.4C05658.

[57] A. Abdelhafiz, B. Wang, A.R. Harutyunyan, J. Li, Carbothermal Shock Synthesis of High Entropy Oxide Catalysts: Dynamic Structural and Chemical Reconstruction Boosting the Catalytic Activity and Stability toward Oxygen Evolution Reaction, Adv. Energy Mater. 12 (2022) 2200742, https://doi.org/10.1002/aenm.202200742.

[58] X. Han, D. Li, J. Zhou, Y. Zheng, L. Kong, L. Li, F. Yan, Electrospun single-phase spinel magnetic high entropy oxide nanoparticles via low-temperature ambient annealing, Nanoscale Adv. 5 (2023) 3075–3083, https://doi.org/10.1039/D3NA00090G.

[59] X. Yang, S. Liping, L. Qiang, H. Lihua, Z. Hui, Co-prosperity of electrocatalytic activity and stability in high entropy spinel (Cr0.2Mn0.2Fe0.2Ni0.2Zn0.2)3O4 for the oxygen evolution reaction, J Mater Chem A Mater 10 (2022) 17633–17641, https://doi.org/10.1039/D2TA01376B.

[60] M. Zhang, J. Ye, Y. Gao, X. Duan, J. Zhao, S. Zhang, X. Lu, K. Luo, Q. Wang, Q. Niu, P. Zhang, S. Dai, General Synthesis of High-Entropy Oxide Nanofibers, ACS Nano 18 (2024) 1449–1463, https://doi.org/10.1021/acsnano.3C07506.

[61] A.T. Tran, V.T. Tran, N.T.M. Nguyet, A.T.Q. Luong, T. Van Le, N.H.H. Phuc, Solid-State Reaction Synthesis of MgAl2O4 Spinel from MgO-Al2O3 Composite Particles Prepared via Electrostatic Adsorption, ACS Omega 8 (2023) 36253–36260, https://doi.org/10.1021/acsomega.3C04782.

[62] H. Yang, G. Chen, J. Ni, S. Praetz, D. Kober, G. Cuello, E. Dal Molin, A. Gili, C. Schlesiger, M.F. Bekheet, D.A.H. Hanaor, A. Gurlo, Synthesis and Electrochemical Performance of High-Entropy Spinel-Type Oxides Derived from Multimetallic Polymeric Precursors, Adv. Energy Sustainability Res. 5 (2024) 2400146, https://doi.org/10.1002/aesr.202400146.

[63] J.M. Kwon, J.H. Kim, S.H. Kang, C.J. Choi, J.A. Rajesh, K.S. Ahn, Facile hydrothermal synthesis of cubic spinel AB2O4 type MnFe2O4 nanocrystallites and their electrochemical performance, Appl. Surf. Sci. 413 (2017) 83–91, https://doi.org/10.1016/j.apsusc.2017.04.022.

[64] S.K. Shaw, A. Gangwar, A. Sharma, S.K. Alla, S. Kavita, M. Vasundhara, S. S. Meena, P. Maiti, N.K. Prasad, Structural and magnetic properties of nanocrystalline equi-atomic spinel high-entropy oxide (AlCoFeMnNi)3O4 synthesised by microwave assisted co-precipitation technique, J. Alloy. Compd. 878 (2021) 160269, https://doi.org/10.1016/j.jallcom.2021.160269.

[65] P. Lesani, A. Babaei, A. Ataie, E. Mostafavi, Nanostructured MnCo2O4 synthesized via co-precipitation method for SOFC interconnect application, Int. J. Hydrogen Energy 41 (2016) 20640–20649, https://doi.org/10.1016/j.ijhydene.2016.07.216.

[66] G.A. El-Shobaky, A.M. Turky, N.Y. Mostafa, S.K. Mohamed, Effect of preparation conditions on physicochemical, surface and catalytic properties of cobalt ferrite prepared by coprecipitation, J. Alloy. Compd. 493 (2010) 415–422, https://doi.org/10.1016/j.jallcom.2009.12.115.

[67] T.X. Nguyen, J. Patra, J.K. Chang, J.M. Ting, High entropy spinel oxide nanoparticles for superior lithiation–delithiation performance, J Mater Chem A Mater 8 (2020) 18963–18973, https://doi.org/10.1039/D0TA04844E.

[68] M.O. Besenhard, A.P. LaGrow, A. Hodzic, M. Kriechbaum, L. Panariello, G. Bais, K. Loizou, S. Damilos, M. Margarida Cruz, N.T.K. Thanh, A. Gavriilidis, Co-precipitation synthesis of stable iron oxide nanoparticles with NaOH: New insights and continuous production via flow chemistry, Chemical Engineering Journal 399 (2020) 125740, https://doi.org/10.1016/j.cej.2020.125740.

[69] A.P. Lagrow, M.O. Besenhard, A. Hodzic, A. Sergides, L.K. Bogart, A. Gavriilidis, N.T.K. Thanh, Unravelling the growth mechanism of the co-precipitation of iron oxide nanoparticles with the aid of synchrotron X-Ray diffraction in solution, Nanoscale 11 (2019) 6620–6628, https://doi.org/10.1039/C9NR00531E.

[70] M.H. Lee, Y.J. Kang, S.T. Myung, Y.K. Sun, Synthetic optimization of Li[Ni1/3Co1/3Mn1/3]O2 via co-precipitation, Electrochim. Acta 50 (2004) 939–948, https://doi.org/10.1016/j.electacta.2004.07.038.

[71] Y. Pei, Q. Chen, Y.C. Xiao, L. Liu, C.Y. Xu, L. Zhen, G. Henkelman, G. Cao, Understanding the phase transitions in spinel-layered-rock salt system: Criterion for the rational design of LLO/spinel nanocomposites, Nano Energy 40 (2017) 566–575, https://doi.org/10.1016/j.nanoen.2017.08.054.

[72] Y. Pei, C.Y. Xu, Y.C. Xiao, Q. Chen, B. Huang, B. Li, S. Li, L. Zhen, G. Cao, Phase Transition Induced Synthesis of Layered/Spinel Heterostructure with Enhanced Electrochemical Properties, Adv. Funct. Mater. 27 (2017) 1604349, https://doi.org/10.1002/adfm.201604349.

[73] H. Yang, L. He, Z. Yang, Q. Chen, G. Jiang, J. Zhu, R. Xue, N. Qiu, Y. Wang, Design optimization of spinel-rocksalt intergrown high entropy oxide structure for enhanced electrochemical properties, J. Alloy. Compd. 968 (2023) 172135, https://doi.org/10.1016/j.jallcom.2023.172135.

[74] D. Hong, Y.H. Choi, High-entropy oxide (Mg0.2Fe0.2Co0.2Cu0.2Zn0.2)O with rocksalt-to-spinel transformation and its electrocatalytic activity for the oxygen evolution reaction, J Alloys Compd 985 (2024) 174029, https://doi.org/10.1016/j.jallcom.2024.174029.

[75] F. Liu, M. Yu, X. Chen, J. Li, H. Liu, F. Cheng, Defective high-entropy rocksalt oxide with enhanced metal-oxygen covalency for electrocatalytic oxygen evolution, Chin. J. Catal. 43 (2022) 122–129, https://doi.org/10.1016/S1872-2067(21)63794-4.

[76] J.Y. Lee, W. Cai, From fabrication to mechanical properties: exploring high-entropy oxide thin films and coatings for high-temperature applications, Frontiers

in Coatings, Dyes and Interface Engineering 2 (2024) 1417527, https://doi.org/10.3389/frcdi.2024.1417527.
[77] M. Fracchia, M. Coduri, P. Ghigna, U. Anselmi-Tamburini, Phase stability of high entropy oxides: A critical review, J. Eur. Ceram. Soc. 44 (2024) 585–594, https://doi.org/10.1016/j.jeurceramsoc.2023.09.056.
[78] X. Xu, H. Yang, R. Tu, S. Liu, J. Hu, Y. Li, Y. Sun, Quenching method to prepare ultra-low loading high-entropy catalyst for furfural selectively hydrogenation at ambient temperature, Appl Catal B 342 (2024) 123358, https://doi.org/10.1016/j.apcatb.2023.123358.
[79] C.C.L. McCrory, S. Jung, J.C. Peters, T.F. Jaramillo, Benchmarking heterogeneous electrocatalysts for the oxygen evolution reaction, J. Am. Chem. Soc. 135 (2013) 16977–16987, https://doi.org/10.1021/ja407115P.
[80] C.C.L. McCrory, S. Jung, I.M. Ferrer, S.M. Chatman, J.C. Peters, T.F. Jaramillo, Benchmarking Hydrogen Evolving Reaction and Oxygen Evolving Reaction Electrocatalysts for Solar Water Splitting Devices, J. Am. Chem. Soc. 137 (2015) 4347–4357, https://doi.org/10.1021/ja510442P.
[81] N. Ullah, W. Zhao, X. Lu, C.J. Oluigbo, S.A. Shah, M. Zhang, J. Xie, Y. Xu, In situ growth of M-MO (M = Ni, Co) in 3D graphene as a competent bifunctional electrocatalyst for OER and HER, Electrochim. Acta 298 (2019) 163–171, https://doi.org/10.1016/j.electacta.2018.12.053.
[82] N. Kirti, P.S. Nandha, D.N. Singh, Srivastava, Improved OER Performance on the Carbon Composite Electrode through Tailored Wettability, ACS Appl Energy Mater 4 (2021) 9618–9626, https://doi.org/10.1021/acsaem.1C01692.
[83] J. Zhang, M. Ren, L. Wang, Y. Li, B.I. Yakobson, J.M. Tour, J. Zhang, M. Ren, Y. Li, B.I. Yakobson, J.M. Tour, L. Wang, Oxidized Laser-Induced Graphene for Efficient Oxygen Electrocatalysis, Adv. Mater. 30 (2018) 1707319, https://doi.org/10.1002/adma.201707319.
[84] A. Caprì, I. Gatto, C. Lo Vecchio, V. Baglio, Effect of the calcination temperature on the characteristics of Ni/Fe-oxide electrocatalysts for application in anion exchange membrane electrolysers, Industrial Chemistry & Materials 1 (2023) 553–562, https://doi.org/10.1039/D3IM00065F.
[85] B. Talluri, M.L. Aparna, N. Sreenivasulu, S.S. Bhattacharya, T. Thomas, High entropy spinel metal oxide (CoCrFeMnNi)3O4 nanoparticles as a high-performance supercapacitor electrode material, J Energy Storage 42 (2021) 103004, https://doi.org/10.1016/j.est.2021.103004.
[86] A. Ashok, A. Kumar, R.R. Bhosale, M.A.H. Saleh, L.J.P. Van Den Broeke, Cellulose assisted combustion synthesis of porous Cu-Ni nanopowders, RSC Adv. 5 (2015) 28703–28712, https://doi.org/10.1039/C5RA03103F.
[87] N.V. Shtertser, L.M. Plyasova, E.V. Dokuchits, T.P. Minyukova, T.M. Yurieva, Thermal decomposition of hydroxycarbonate Cu-Fe-Cr spinel precursors, Catalysis for Sustainable, Energy 4 (2017) 67–72, https://doi.org/10.1515/cse-2017-0011.
[88] J. Sicklinger, M. Metzger, H. Beyer, D. Pritzl, H.A. Gasteiger, Ambient Storage Derived Surface Contamination of NCM811 and NCM111: Performance Implications and Mitigation Strategies, J. Electrochem. Soc. 166 (2019) A2322–A2335, https://doi.org/10.1149/2.0011912jes.
[89] A. Ratnawulan, S.H. Fauzi, Ae, Effect of calcination temperature on phase transformation and crystallite size of copper oxide (CuO) powders, AIP Conference Proceedings 1868 (2017), https://doi.org/10.1063/1.4995173.
[90] A.H. Shah, M.A. Rather, Effect of calcination temperature on the crystallite size, particle size and zeta potential of TiO2 nanoparticles synthesized via polyol-mediated method, Mater. Today Proc. 44 (2021) 482–488, https://doi.org/10.1016/j.matpr.2020.10.199.
[91] J.C. Chen, W.C. Chen, Y.C. Tien, C.J. Shih, Effect of calcination temperature on the crystallite growth of cerium oxide nano-powders prepared by the co-precipitation process, J. Alloy. Compd. 496 (2010) 364–369, https://doi.org/10.1016/j.jallcom.2010.01.151.
[92] L. Merabet, K. Rida, N. Boukmouche, Sol-gel synthesis, characterization, and supercapacitor applications of MCo2O4 (M = Ni, Mn, Cu, Zn) cobaltite spinels, Ceram. Int. 44 (2018) 11265–11273, https://doi.org/10.1016/j.ceramint.2018.03.171.
[93] C.Q. Duan, K. Tian, X. Li, D. Wang, H. Sun, R. Zheng, Z. Wang, Y. Liu, New spinel high-entropy oxides (FeCoNiCrMnXLi)3O4 (X = Cu, Mg, Zn) as the anode material for lithium-ion batteries, Ceram. Int. 47 (2021) 32025–32032, https://doi.org/10.1016/j.ceramint.2021.08.091.
[94] K. Gu, D. Wang, C. Xie, T. Wang, G. Huang, Y. Liu, Y. Zou, L. Tao, S. Wang, Defect-Rich High-Entropy Oxide Nanosheets for Efficient 5-Hydroxymethylfurfural Electrooxidation, Angew. Chem. 133 (2021) 20415–20420, https://doi.org/10.1002/ange.202107390.
[95] T.X. Nguyen, C.C. Tsai, J. Patra, O. Clemens, J.K. Chang, J.M. Ting, Co-free high entropy spinel oxide anode with controlled morphology and crystallinity for outstanding charge/discharge performance in Lithium-ion batteries, Chem. Eng. J. 430 (2022) 132658, https://doi.org/10.1016/j.cej.2021.132658.
[96] D. Wang, Z. Liu, S. Du, Y. Zhang, H. Li, Z. Xiao, W. Chen, R. Chen, Y. Wang, Y. Zou, S. Wang, Low-temperature synthesis of small-sized high-entropy oxides for water oxidation, J Mater Chem A Mater 7 (2019) 24211–24216, https://doi.org/10.1039/C9TA08740K.
[97] F. Song, M.M. Busch, B. Lassalle-Kaiser, C.S. Hsu, E. Petkucheva, M. Bensimon, H. M. Chen, C. Corminboeuf, X. Hu, An Unconventional Iron Nickel Catalyst for the Oxygen Evolution Reaction, ACS Cent. Sci. 5 (2019) 558–568, https://doi.org/10.1021/acscentsci.9B00053.
[98] T.D. Sparks, A. Gurlo, M.F. Bekheet, M.W. Gaultois, G. Cherkashinin, L. Laversenne, D.R. Clarke, High-temperature structure of Co3 O4: Understanding spinel inversion using in situ and ex situ measurements, Phys. Rev. B 99 (2019) 104104, https://doi.org/10.1103/physrevb.99.104104.
[99] Q. Feng, Y. Sun, H. He, J. Zhao, F. Meng, F.X. Wang, D. Zheng, G. Wang, F. Deng, N. Yi, B. Jin, Quenching-induced surface engineering of ZnCo2O4 spinel oxide for enhanced oxygen evolution reaction, Appl. Surf. Sci. 611 (2023) 155662, https://doi.org/10.1016/j.apsusc.2022.155662.
[100] H. Sun, X. Xu, Y. Song, W. Zhou, Z. Shao, H. Sun, Y. Song, W. Zhou, Z. Shao, X. Xu, Designing High-Valence Metal Sites for Electrochemical Water Splitting, Adv. Funct. Mater. 31 (2021) 2009779, https://doi.org/10.1002/adfm.202009779.
[101] Z.W. She, J. Kibsgaard, C.F. Dickens, I. Chorkendorff, J.K. Nørskov, T.F. Jaramillo, Combining theory and experiment in electrocatalysis: Insights into materials design, Science (1979) 355 (2017). https://doi.org/10.1126/science.aad4998.
[102] P.L. Mahapatra, A.K. Singh, R. Tromer, P. Kumbhakar, S.K. Sinha, B. Lahiri, T. K. Kundu, D.S. Galvao, C.S. Tiwary, Energy harvesting using two-dimensional magnesiochromite (MgCr2O4), Mater. Today Nano 23 (2023) 100374, https://doi.org/10.1016/j.mtnano.2023.100374.
[103] A.I. Ikeuba, B. Zhang, J. Wang, E.-H. Han, W. Ke, P.C. Okafor, SVET and SIET Study of Galvanic Corrosion of Al/MgZn 2 in Aqueous Solutions at Different pH, J. Electrochem. Soc. 165 (2018) C180–C194, https://doi.org/10.1149/2.0861803jes.
[104] M. Stygar, J. Dąbrowa, M. Moździerz, M. Zajusz, W. Skubida, K. Mroczka, K. Berent, K. Świerczek, M. Danielewski, Formation and properties of high entropy oxides in Co-Cr-Fe-Mg-Mn-Ni-O system: Novel (Cr,Fe,Mg,Mn,Ni)3O4 and (Co,Cr,Fe,Mg,Mn)3O4 high entropy spinels, J. Eur. Ceram. Soc. 40 (2020) 1644–1650, https://doi.org/10.1016/j.jeurceramsoc.2019.11.030.
[105] M.W. Roberts, R.S.C. Smart, The defect structure of nickel oxide surfaces as revealed by photoelectron spectroscopy, J. Chem. Soc., Faraday Trans. 1 80 (1984) 2957–2968, https://doi.org/10.1039/F19848002957.
[106] M.C. Biesinger, L.W.M. Lau, A.R. Gerson, R.S.C. Smart, The role of the Auger parameter in XPS studies of nickel metal, halides and oxides, PCCP 14 (2012) 2434–2442, https://doi.org/10.1039/C2CP22419D.
[107] C. Duan, X. Li, D. Wang, Z. Wang, H. Sun, R. Zheng, Y. Liu, Nanosized high entropy spinel oxide (FeCoNiCrMn)3O4 as a highly active and ultra-stable electrocatalyst for the oxygen evolution reaction, Sustain, Energy Fuels 6 (2022) 1479–1488, https://doi.org/10.1039/D1SE02038B.
[108] H. Meng, Y. Liu, H. Liu, S. Pei, X. Yuan, H. Li, Y. Zhang, ZIF67@MFC-Derived Co/N-C@CNFs Interconnected Frameworks with Graphitic Carbon-Encapsulated Co Nanoparticles as Highly Stable and Efficient Electrocatalysts for Oxygen Reduction Reactions, ACS Appl. Mater. Interfaces 12 (2020) 41580–41589, https://doi.org/10.1021/acsami.0c12069.
[109] J. Zhu, Q. Gao, Mesoporous MCo2O4 (M = Cu, Mn and Ni) spinels: Structural replication, characterization and catalytic application in CO oxidation, Microporous Mesoporous Mater. 124 (2009) 144–152, https://doi.org/10.1016/j.micromeso.2009.05.003.
[110] W. Wei, W. Chen, D.G. Ivey, Rock salt-spinel structural transformation in anodically electrodeposited Mn-Co-O nanocrystals, Chem. Mater. 20 (2008) 1941–1947, https://doi.org/10.1021/cm703464P.
[111] S. Zafeiratos, T. Dintzer, D. Teschner, R. Blume, M. Hävecker, A. Knop-Gericke, R. Schlögl, Methanol oxidation over model cobalt catalysts: Influence of the cobalt oxidation state on the reactivity, J. Catal. 269 (2010) 309–317, https://doi.org/10.1016/j.jcat.2009.11.013.
[112] M. Mullet, V. Khare, C. Ruby, XPS study of Fe(II)-Fe(III) (oxy)hydroxycarbonate green rust compounds, Surf. Interface Anal. 40 (2008) 323–328, https://doi.org/10.1002/sia.2758.
[113] M. Descostes, F. Mercier, N. Thromat, C. Beaucaire, M. Gautier-Soyer, Use of XPS in the determination of chemical environment and oxidation state of iron and sulfur samples: constitution of a data basis in binding energies for Fe and S reference compounds and applications to the evidence of surface species of an oxidized pyrite in a carbonate medium, Appl. Surf. Sci. 165 (2000) 288–302, https://doi.org/10.1016/S0169-4332(00)00443-8.
[114] A. Machet, A. Galtayries, P. Marcus, P. Combrade, P. Jolivet, P. Scott, XPS study of oxides formed on nickel-base alloys in high-temperature and high-pressure water, Surf. Interface Anal. 34 (2002) 197–200, https://doi.org/10.1002/sia.1282.
[115] A.G. Sault, Quantitative analysis of Auger lineshapes of oxidized iron, Appl. Surf. Sci. 74 (1994) 249–262, https://doi.org/10.1016/0169-4332(94)90006-X.
[116] E.S. Ilton, J.E. Post, P.J. Heaney, F.T. Ling, S.N. Kerisit, XPS determination of Mn oxidation states in Mn (hydr)oxides, Appl. Surf. Sci. 366 (2016) 475–485, https://doi.org/10.1016/j.apsusc.2015.12.159.
[117] R. Grissa, H. Martinez, S. Cotte, J. Galipaud, B. Pecquenard, F. Le Cras, Thorough XPS analyses on overlithiated manganese spinel cycled around the 3V plateau, Appl. Surf. Sci. 411 (2017) 449–456, https://doi.org/10.1016/j.apsusc.2017.03.205.
[118] Y. Liu, C. Ye, L. Chen, J. Fan, C. Liu, L. Xue, J. Sun, W. Zhang, X. Wang, P. Xiong, J. Zhu, High Entropy-Driven Role of Oxygen Vacancies for Water Oxidation, Adv. Funct. Mater. 34 (2024) 2314820, https://doi.org/10.1002/adfm.202314820.
[119] Y. Wu, C. Guo, R. Yao, K. Zhang, J. Li, G. Liu, Modulating Carrier Oxygen Vacancies to Enhance Strong Oxide-Support Interaction in IrO2/Nb2O5-x Catalysts for Promoting Acidic Oxygen Evolution Reaction, Adv. Funct. Mater. 34 (2024) 2410193, https://doi.org/10.1002/adfm.202410193.
[120] Z. Wang, R. Lin, Y. Huo, H. Li, L. Wang, Formation, Detection, and Function of Oxygen Vacancy in Metal Oxides for Solar Energy Conversion, Adv. Funct. Mater. 32 (2022) 2109503, https://doi.org/10.1002/adfm.202109503.
[121] K. An, Z. Yu, H. Bai, D. Liu, L. Qiao, X. Lv, L. Shao, J. Feng, Y. Cao, L. Li, Z. Wen, S. Chen, Z. Pan, S. Wang, H. Pan, Oxygen vacancy redistribution and ferroelectric polarization relaxation on epitaxial perovskite films during an electrocatalytic

process, J Mater Chem A Mater 12 (2024) 9672–9680, https://doi.org/10.1039/D3TA07815A.
[122] H. Li, L. Hansen, A. Aliyeva, J. Wang, H. Qiu, M. Müller, S. Chen, C. Aktas, L. Kienle, B. Hartke, J. Benedikt, Plasma-engineering of Pt-decorated NiCo2O4 nanowires with rich oxygen vacancies for enhanced oxygen electrocatalysis and zinc-air battery performance, Applied Catalysis b: Environment and Energy 361 (2025) 124607, https://doi.org/10.1016/j.apcatb.2024.124607.
[123] Y. Song, X. Meng, M. Bi, W. Gao, Effect of hydroxyl groups on the oxygen vacancy and hydrogen-sensitive properties of CeO2 in different morphologies, Int. J. Hydrogen Energy 47 (2022) 25443–25453, https://doi.org/10.1016/j.ijhydene.2022.05.255.
[124] E. Marelli, J. Gazquez, E. Poghosyan, E. Müller, D.J. Gawryluk, E. Pomjakushina, D. Sheptyakov, C. Piamonteze, D. Aegerter, T.J. Schmidt, M. Medarde, E. Fabbri, Correlation between Oxygen Vacancies and Oxygen Evolution Reaction Activity for a Model Electrode: PrBaCo2O5+δ, Angew. Chem. Int. Ed. 60 (2021) 14609–14619, https://doi.org/10.1002/anie.202103151.
[125] Z. Xiao, Y. Wang, Y.C. Huang, Z. Wei, C.L. Dong, J. Ma, S. Shen, Y. Li, S. Wang, Filling the oxygen vacancies in Co3O4 with phosphorus: an ultra-efficient electrocatalyst for overall water splitting, Energy, Environ. Sci. 10 (2017) 2563–2569, https://doi.org/10.1039/C7EE01917C.
[126] M. Harada, F. Kotegawa, M. Kuwa, Structural Changes of Spinel MCo2O4(M = Mn, Fe, Co, Ni, and Zn) Electrocatalysts during the Oxygen Evolution Reaction Investigated by in Situ X-ray Absorption Spectroscopy, ACS Appl. Energy Mater. 5 (2022) 278–294, https://doi.org/10.1021/acsaem.1C02824.
[127] X. Deng, S. Öztürk, C. Weidenthaler, H. Tüysüz, Iron-Induced Activation of Ordered Mesoporous Nickel Cobalt Oxide Electrocatalyst for the Oxygen Evolution Reaction, ACS Appl. Mater. Interfaces 9 (2017) 21225–21233, https://doi.org/10.1021/acsami.7B02571.
[128] H.Y. Wang, Y.Y. Hsu, R. Chen, T.S. Chan, H.M. Chen, B. Liu, Ni3+-induced formation of active NiOOH on the spinel Ni-Co oxide surface for efficient oxygen evolution reaction, Adv. Energy Mater. 5 (2015), https://doi.org/10.1002/aenm.201500091.
[129] O. Diaz-Morales, D. Ferrus-Suspedra, M.T.M. Koper, The importance of nickel oxyhydroxide deprotonation on its activity towards electrochemical water oxidation, Chem. Sci. 7 (2016) 2639–2645, https://doi.org/10.1039/C5SC04486C.
[130] A.C. Garcia, T. Touzalin, C. Nieuwland, N. Perini, M.T.M. Koper, Enhancement of Oxygen Evolution Activity of Nickel Oxyhydroxide by Electrolyte Alkali Cations, Angew. Chem. 131 (2019) 13133–13137, https://doi.org/10.1002/ange.201905501.
[131] H. Zhong, Q. Zhang, J. Yu, X. Zhang, C. Wu, Y. Ma, H. An, H. Wang, J. Zhang, X. Wang, J. Xue, H. Zhong, Q. Zhang, J. Yu, X. Zhang, Y. Ma, H. An, H. Wang, J. Zhang, X. Wang, J. Xue, C. Wu, Fundamental Understanding of Structural Reconstruction Behaviors in Oxygen Evolution Reaction Electrocatalysts, Adv. Energy Mater. 13 (2023) 2301391, https://doi.org/10.1002/aenm.202301391.
[132] M. Ning, F. Zhang, L. Wu, X. Xing, D. Wang, S. Song, Q. Zhou, L. Yu, J. Bao, S. Chen, Z. Ren, Boosting efficient alkaline fresh water and seawater electrolysis via electrochemical reconstruction, Energy, Environ. Sci. 15 (2022) 3945–3957, https://doi.org/10.1039/D2EE01094A.
[133] S. Wang, W. Huo, F. Fang, Z. Xie, J.K. Shang, J. Jiang, High entropy alloy/C nanoparticles derived from polymetallic MOF as promising electrocatalysts for alkaline oxygen evolution reaction, Chem. Eng. J. 429 (2022) 132410, https://doi.org/10.1016/j.cej.2021.132410.
[134] T. Wu, S. Sun, J. Song, S. Xi, Y. Du, B. Chen, W.A. Sasangka, H. Liao, C.L. Gan, G. G. Scherer, L. Zeng, H. Wang, H. Li, A. Grimaud, Z.J. Xu, Iron-facilitated dynamic active-site generation on spinel CoAl2O4 with self-termination of surface reconstruction for water oxidation, Nature Catalysis 2019 2:9 2 (2019) 763–772. https://doi.org/10.1038/s41929-019-0325-4.
[135] G. Zhang, Z. Li, J. Zeng, L. Yu, C. Zuo, P. Wen, Y. Liu, L. Zhong, H. Chen, Y. Qiu, Ferric ions leached from Fe-based catalyst to trigger the dynamic surface reconstruction of nickel foam for high-efficient OER activity, Appl Catal B 319 (2022) 121921, https://doi.org/10.1016/j.apcatb.2022.121921.
[136] B. Han, A. Grimaud, L. Giordano, W.T. Hong, O. Diaz-Morales, L. Yueh-Lin, J. Hwang, N. Charles, K.A. Stoerzinger, W. Yang, M.T.M. Koper, Y. Shao-Horn, Iron-Based Perovskites for Catalyzing Oxygen Evolution Reaction, J. Phys. Chem. C 122 (2018) 8445–8454, https://doi.org/10.1021/acs.jpcc.8B01397.
[137] B. He, P. Hosseini, D. Escalera-López, J. Schulwitz, O. Rüdiger, U. Hagemann, M. Heidelmann, S. DeBeer, M. Muhler, S. Cherevko, K. Tschulik, T. Li, Effects of Dynamic Surface Transformation on the Activity and Stability of Mixed Co-Mn Cubic Spinel Oxides in the Oxygen Evolution Reaction in Alkaline Media, Adv. Energy Mater. (2024) 2403096, https://doi.org/10.1002/aenm.202403096.
[138] E.S. Da Silva, A. Macili, R. Bofill, J. García-Antón, X. Sala, L. Francàs, Boosting the Oxygen Evolution Activity of FeNi Oxides/Hydroxides by Molecular and Atomic Engineering, Chemistry – A, European Journal 30 (2024) e202302251, https://doi.org/10.1002/chem.202302251.
[139] Y. Zhou, N. López, The Role of Fe Species on NiOOH in Oxygen Evolution Reactions, ACS Catal. 10 (2020) 6254–6261, https://doi.org/10.1021/acscatal.0C00304.
[140] S. Klaus, Y. Cai, M.W. Louie, L. Trotochaud, A.T. Bell, Effects of Fe electrolyte impurities on Ni(OH)2/NiOOH structure and oxygen evolution activity, J. Phys. Chem. C 119 (2015) 7243–7254, https://doi.org/10.1021/acs.jpcc.5B00105.
[141] O. van der Heijden, S. Park, R.E. Vos, J.J.J. Eggebeen, M.T.M. Koper, Tafel Slope Plot as a Tool to Analyze Electrocatalytic Reactions, ACS Energy Lett. 9 (2024) 1871–1879, https://doi.org/10.1021/acsenergylett.4C00266.
[142] M.S. Burke, M.G. Kast, L. Trotochaud, A.M. Smith, S.W. Boettcher, Cobalt-Iron (Oxy)hydroxide Oxygen Evolution Electrocatalysts: The Role of Structure and Composition on Activity, Stability, and Mechanism, J. Am. Chem. Soc. 137 (2015) 3638–3648, https://doi.org/10.1021/jacs.5B00281.
[143] A. Grimaud, O. Diaz-Morales, B. Han, W.T. Hong, Y.L. Lee, L. Giordano, K.A. Stoerzinger, M.T.M. Koper, Y. Shao-Horn, Activating lattice oxygen redox reactions in metal oxides to catalyse oxygen evolution, Nature Chemistry 2017 9: 5 9 (2017) 457–465. https://doi.org/10.1038/nchem.2695.
[144] A. Moysiadou, S. Lee, C.S. Hsu, H.M. Chen, X. Hu, Mechanism of Oxygen Evolution Catalyzed by Cobalt Oxyhydroxide: Cobalt Superoxide Species as a Key Intermediate and Dioxygen Release as a Rate-Determining Step, J. Am. Chem. Soc. 142 (2020) 11901–11914, https://doi.org/10.1021/jacs.0C04867.
[145] S. Lee, K. Banjac, M. Lingenfelder, X. Hu, Oxygen Isotope Labeling Experiments Reveal Different Reaction Sites for the Oxygen Evolution Reaction on Nickel and Nickel Iron Oxides, Angew. Chem. Int. Ed. 58 (2019) 10295–10299, https://doi.org/10.1002/anie.201903200.
[146] R.R. Katzbaer, F.M. dos Santos Vieira, I. Dabo, Z. Mao, R.E. Schaak, Band Gap Narrowing in a High-Entropy Spinel Oxide Semiconductor for Enhanced Oxygen Evolution Catalysis, J Am Chem Soc 145 (2023) 6753–6761, https://doi.org/10.1021/jacs.2C12887.
[147] A. Martinez-Lazaro, A. Caprì, I. Gatto, J. Ledesma-García, N. Rey-Raap, A. Arenillas, F.I. Espinosa-Lagunes, V. Baglio, L.G. Arriaga, NiFe2O4 hierarchical nanoparticles as electrocatalyst for anion exchange membrane water electrolysis, J. Power Sources 556 (2023) 232417, https://doi.org/10.1016/j.jpowsour.2022.232417.
[148] W. Hooch Antink, S. Lee, H.S. Lee, H. Shin, T.Y. Yoo, W. Ko, J. Shim, G. Na, Y. E. Sung, T. Hyeon, High-Valence Metal-Driven Electronic Modulation for Boosting Oxygen Evolution Reaction in High-Entropy Spinel Oxide, Adv. Funct. Mater. 34 (2024) 2309438, https://doi.org/10.1002/adfm.202309438.
[149] J. Wang, J. Zhang, H. Yu, L. Chen, H. Jiang, C. Li, Strain Engineering of High-Entropy Oxides Enriches Highly Active Lattice Oxygen for Electrocatalytic Water Oxidation, ACS Mater. Lett. 6 (2024) 1739–1745, https://doi.org/10.1021/acsmaterialslett.4C00286.
[150] A. Caprì, A. Martínez-Lázaro, J. Béjar, I. Gatto, L. Álvarez-Contreras, M. P. Gurrola, J. Ledesma-García, V. Baglio, L.G. Arriaga, Three-dimensionally ordered macroporous trimetallic spinel for anion exchange membrane water electrolysis, Electrochim. Acta 463 (2023) 142851, https://doi.org/10.1016/j.electacta.2023.142851.
[151] A. Martínez-Lázaro, F.I. Espinosa-Lagunes, A. Molina, G. Luna-Bárcenas, C. Lo Vecchio, I. Gatto, A. Arenillas, V. Baglio, J. Ledesma-García, L. Arriaga, Fenico Aerogel for Oxygen Evolution Reaction in Alkaline Systems: Microfluidic and Anion Exchange Membrane Electrolyzers, (n.d.). https://doi.org/10.2139/ssrn.4773647.
[152] J.E. Park, M.J. Kim, M.S. Lim, S.Y. Kang, J.K. Kim, S.H. Oh, M. Her, Y.H. Cho, Y. E. Sung, Graphitic carbon nitride-carbon nanofiber as oxygen catalyst in anion-exchange membrane water electrolyzer and rechargeable metal–air cells, Appl Catal B 237 (2018) 140–148, https://doi.org/10.1016/j.apcatb.2018.05.073.
[153] S. Li, T. Liu, W. Zhang, M. Wang, H. Zhang, C. Qin, L. Zhang, Y. Chen, S. Jiang, D. Liu, X. Liu, H. Wang, Q. Luo, T. Ding, T. Yao, Highly efficient anion exchange membrane water electrolyzers via chromium-doped amorphous electrocatalysts, Nature Communications 2024 15:1 15 (2024) 1–11. https://doi.org/10.1038/s41467-024-47736-0.
[154] T. Caielli, A.R. Ferrari, S. Bonizzoni, E. Sediva, A. Caprì, M. Santoro, I. Gatto, V. Baglio, P. Mustarelli, Synthesis, characterization and water electrolyzer cell tests of poly(biphenyl piperidinium) Anion exchange membranes, J. Power Sources 557 (2023) 232532, https://doi.org/10.1016/j.jpowsour.2022.232532.